

Towards Robust Drone Vision in the Wild

Master Thesis

By the student

Xiaoyu Lin

Approved by the Examining Committee:

Prof. Süssstrunk Sabine, Thesis Advisor

Prof. Nasrollahi Kamal, External Expert

Dr. Majed El Helou, Thesis Supervisor



Image and Visual Representation Lab
School of Computer and Communication Sciences
Lausanne, EPFL, 2022

Abstract

The past few years have witnessed the burst of drone-based applications where computer vision plays an essential role. However, most public drone-based vision datasets focus on detection and tracking. On the other hand, the performance of most existing image super-resolution methods is sensitive to the dataset, specifically, the degradation model between high-resolution and low-resolution images. In this thesis, we propose the first image super-resolution dataset for drone vision. Image pairs are captured by two cameras on the drone with different focal lengths. We collect data at different altitudes and then propose pre-processing steps to align image pairs. Extensive empirical studies show domain gaps exist among images captured at different altitudes. Meanwhile, the performance of pretrained image super-resolution networks also suffers a drop on our dataset and varies among altitudes. Finally, we propose two methods to build a robust image super-resolution network at different altitudes. The first feeds altitude information into the network through altitude-aware layers. The second uses one-shot learning to quickly adapt the super-resolution model to unknown altitudes. Our results reveal that the proposed methods can efficiently improve the performance of super-resolution networks at varying altitudes.

Key words: drone vision, image super-resolution, domain adaptation, few-shot learning.

Contents

Abstract	i
1 Introduction	1
1.1 Background	1
1.2 Objectives	2
1.3 Thesis organization	4
2 Literature review	5
2.1 Drone vision	5
2.2 Single image super-resolution	6
2.3 Recent advances in image super-resolution dataset	7
2.4 Summary	8
3 Data acquisition	9
3.1 Platform	9
3.1.1 Drone	9
3.1.2 Cameras	9
3.1.3 DJI Fly App	10
3.2 Manual camera settings	11
3.2.1 F-number	11
3.2.2 ISO	13
3.2.3 Shutter	13
3.2.4 Summary of manual mode	13
3.3 Auto camera settings	14
3.4 Compare lower altitude and optical zoom	14
3.5 Comparison between burst frames	15
3.6 Scene selection	16
3.7 Summary	16
4 Data pre-processing	19
4.1 Field of view matching	19
4.2 Local alignment	20
4.3 Color correction	21
4.4 Misalignment analysis	22

4.5 Summary	23
5 Domain gap observation	25
5.1 From synthetic downsampling to real-world degradation	25
5.2 Effects of altitudes on pretrained SISR networks	27
5.3 Effects of altitudes on fine-tuned SISR networks	27
5.4 Analysis	28
5.5 Summary	30
6 Robust model at varying altitudes	35
6.1 Feeding altitude information	35
6.2 Few-shot learning	36
6.3 Analysis	38
6.4 Summary	38
7 Conclusion and future plan	41
A More visual examples	43
A.1 SR matching visualisation	43
A.2 Test samples of fine-tuning	43
A.3 Test samples of robust model for varying altitudes	43
Bibliography	53

1 Introduction

1.1 Background

The history of using drones dates back more than one hundred years ago (Akbari et al., 2021). Since then, drone technology has endured and been developed mainly for military use. In 2006, DJI, a leader company in the commercial and individual drone industry, developed the first commercial drone. After that, the past few years have witnessed the burst of drones for both commercial and private usage.

Compared with other enduring platforms such as airplanes and satellites, drones can obtain higher-resolution images and achieve better low-altitude maneuverability. It can fly at various speeds indoors or outdoors and control its position, making it an ideal substitute for humans in certain situations, like exploring dangerous places. Moreover, as a platform, the drone can be mounted with multiple sensors and used for different tasks. For example, a drone with sensors to detect its surroundings can automatically avoid obstacles while flying in complicated environments. Most importantly, the drone is much cheaper for maintenance. However, due to the constraint of battery life, the drone can only work continuously for less than a few hours and thus can only cover a small area. More detailed comparisons between the drone and other platforms are listed in Table 1.1.

In recent years, the powerful features of drones have been continuously improved. Thus, drones have been applied in many fields, such as security and surveillance, agriculture and

	Drones	Helicopter/Airplane	Satellite
Operating cost	Low	Moderate	High
Resolution	Very high	Very high	High
Low altitude maneuverability	High	Moderate	Poor
Geographic coverage	Localized	Regional	Entire planet
Continuous working time	Short	Moderate	Long
Operation	Easy	Hard	Hard

Table 1.1: Comparison between the drone and its alternatives.

forest, and disaster detection. Furthermore, computer vision methods play an essential role in most drone applications. Analyzing video or images captured by drones has become an emerging application attracting significant attention from researchers in various domains of computer vision.

Computer vision aims at deriving meaningful information from digital images, videos, and other visual inputs. Most existing research in drone vision focuses on object detection and tracking (Du et al., 2018; Yu et al., 2020; Zhu et al., 2018), drone-autonomous navigation such as flight control and visual localization, or some challenges related to remote sensing like camera calibration (Y. Xu et al., 2016). On the other hand, one of the essential areas in computer vision and image processing is image super-resolution (SR). However, limited drone vision datasets are proposed, and most public drone vision datasets focus only on one or two specific tasks, such as object detection (Du et al., 2018; Yu et al., 2020; Zhu et al., 2018). To the best of our knowledge, none has offered a drone vision dataset for the image SR task. Consequently, developing a drone vision benchmark for the image SR is of great importance to boosting related research.

The target of single image super-resolution (SISR) is to recover the high-resolution (HR) image from low-resolution (LR) observation. Recently, learning-based methods (Bhat et al., 2021; Dong et al., 2014; L. Wang, Wang, Dong, et al., 2021; L. Wang, Wang, Lin, et al., 2021) have dominated the research of SISR due to the impressive feature extraction capability of deep neural networks, especially convolutional neural networks (CNN). However, most existing methods are trained and evaluated on synthetic datasets. The LR images are generated by applying a simple and uniform degradation (i.e., MATLAB bicubic downsampling) to HR images. Recently, some researchers (Cai, Zeng, et al., 2019; L. Wang, Wang, Dong, et al., 2021) have found that those methods suffer a severe performance drop when applied in a real-world scenario, as the degradation model is more complex in the real-world. It is thus highly desired that we can have a training dataset consisting of real-world, instead of synthetic, LR and HR image pairs (Cai, Zeng, et al., 2019). Therefore, some real-world SR datasets have been proposed (Bhat et al., 2021; Cai, Gu, et al., 2019; Cai, Zeng, et al., 2019; X. Zhang et al., 2019). However, all of them are captured on the ground using digital single-lens reflex (DSLR) cameras or mobile phones. Still, the image degradation model is different among different devices and scenarios, which means these datasets can not apply to drone vision.

1.2 Objectives

In this project, we aim to construct a general and real-world dataset of images captured by the drone's bird-view for the image SR task. To the best of our knowledge, no one has provided a drone vision dataset for image SR. Constructing such a drone vision super-resolution (DroneSR) dataset is non-trivial because perfectly aligned LR and HR image pairs are tough to acquire. Therefore, we propose a more flexible procedure for data acquisition. More specifically, we use a drone equipped with two cameras with different focal lengths. We capture

images of the same scene using two cameras one by one. The image captured by the camera with a larger focal length is regarded as our HR ground-truth, and the image captured by the other camera is our LR image. In this way, HR and LR image pairs on different resolutions can be collected. However, in addition to the change of field of view (FoV), using two cameras can result in many other challenges in image processing, such as a change of optical center and a change of camera settings. To solve this problem, we first develop an FoV matching algorithm to find matched FoV in LR images. Then we apply local alignment on LR and HR image patches to eliminate misalignment. Finally, we propose a color correction algorithm to match the RGB color in LR and HR image pairs.

Since the texture and content of images are captured at different altitudes, we collect LR and HR image pairs at ten different altitudes in each scene. Recently, researchers found that using RAW data as SR model input can improve the performance of the SR model. Another way to enhance SR performance is to use burst sequence images as input since different burst frames may contain subpixel information (Bhat et al., 2021; Dudhane et al., 2021; Lecouat et al., 2021). Researchers in the SR area are also interested in building an SR model for the arbitrary scale factor. Therefore, we also collect RAW data for HR and LR images and enable burst mode when capturing LR images to benefit others who want to use our dataset for further research.

Our DroneSR dataset contains HR and LR image pairs at different altitudes. We then evaluate existing SR models on our dataset and find that those methods' performance varies among altitudes. This is caused by the texture and content differences at various altitudes. Specifically, we found that images captured at lower altitudes contain more high-frequency details (see Figure 5.2). Since the altitude information is available in our dataset, we propose a new method to feed the altitude information into SR models to build a robust SR model for drone vision at varying altitudes. Finally, we try to apply a few-shot learning setting to our DroneSR dataset and image SR model, so the SR model trained on some altitudes can be quickly adapted to new altitudes.

The object of this project is to propose the first drone vision dataset for image SR and make the image super-resolution methods robust for drone vision at varying altitudes; therefore, the drone can fly higher and still work. To achieve the target, some tasks are identified:

- To build a drone vision dataset consisting of LR-HR images at different altitudes;
- To benchmark state-of-the-art (SOTA) SR models based on our dataset and evaluate the domain gap between standard datasets and our dataset.
- To propose methods to make image SR models robust for drone vision at various altitudes.

1.3 Thesis organization

This thesis consists of seven chapters in the main body, and it is structured as follows. After this introductory chapter, the second chapter briefly reviews the history of drone vision and image SR. The detailed procedures for data acquisition are introduced in the third chapter. The fourth chapter focuses on the pre-processing steps to generate well-aligned image pairs for SR. Extensive empirical studies in the fifth chapter show domain gaps exist among images captured from different altitudes. We propose two methods to build a robust image super-resolution network at different altitudes in the sixth chapter.

In the last chapter, the conclusion of the proposed dataset and methods, as well as some plans and suggestions for further research, are discussed.

2 Literature review

The last few years have witnessed a burst of drone technology and significant improvement in image SR. This chapter firstly gives a brief overview of drone vision. Then we review several important works for learning-based SISR. Finally, we review some recent advances in the image SR dataset.

2.1 Drone vision

Over the past few years, drones are rapidly growing in popularity due to their low altitude maneuverability, low maintenance cost, and easy operation. As a result, they have become central to the platform of various applications, ranging from military security and academic research to daily life. Computer vision methods play an essential role in those drone applications. Those applications can be grouped into three categories. The first group is related to remote-sensing, such as camera calibration and image matching (Y. Xu et al., 2016). The second group related to drones' automating flight and stabilization, including pose estimation and obstacle detection, which is an essential feature of a modern drone. Recently, drone companies have used vision systems for this (Al-Kaff et al., 2018).

Compared with the previous two groups, the applications of images and videos captured by drones attract more attention. Some drone-based image or video datasets have been developed for specific tasks such as traffic and crowd detection (Liu and Mattyus, 2015; Oh et al., 2011) for surveillance. The acquired images by drones may be under different ambient conditions in that dataset. As one of the main areas in computer vision, object detection aims to detect instances of semantic objects of a specific class in images or videos. Recently, more and more drone-based image and video dataset has been proposed for object detection task (Hsieh et al., 2017; X. Xu et al., 2019). The UAVDT (Du et al., 2018) benchmark is a viral database for the object detection and tracking using drone images. This dataset also contains some real-world challenges, such as various weather conditions, flying altitudes, and drone views.

Large datasets can be used to evaluate conventional approaches and apply new methods, especially for learning-based computer vision methods. However, in recent years, although researchers have developed plenty of datasets for drone-based vision, most of them only focus on object detection and other related tasks. In addition, few works provided publicly available datasets for other computer vision tasks, such as image super-resolution, which requires more effort.

2.2 Single image super-resolution

Traditionally, SISR methods (Chang et al., 2004; Timofte et al., 2013) are based on exemplar or dictionary. These methods generate HR images by leveraging the related patches in a large external database. Therefore, the performance of those methods is restricted by the size and content of the external database. Besides, those methods usually take a lot of time for inference.

With the rapid development of deep learning, learning-based methods have achieved notable improvements over early SR methods and dominated the research of SISR because those methods can extract rich feature representations from images. As a pioneer work, SRCNN (Dong et al., 2014) was firstly proposed using a three-layer architecture to learn LR and HR relationships. The SRCNN needs to upscale the LR image to the target size using bicubic interpolation before feeding it into the network. After that, more CNN-based methods have been proposed. VDSR (Kim et al., 2016a) and DRCN (Kim et al., 2016b) achieved significant improvement over SRCNN by increasing the depth of the network to 20 and using residual learning and recursive learning to speed up training. Following the idea of residual learning, EDSR (Lim et al., 2017) was proposed with a very wide architecture, and a very deep one MDSR (Lim et al., 2017) was also proposed with simplified residual blocks. After that, DRRN (Tai, Yang, and Liu, 2017) was proposed by introducing recursive blocks with shared parameters for stable training. Then a persistent memory network called Memnet (Tai, Yang, Liu, and Xu, 2017) was developed for the SISR task. Combining residual learning and densely connected block, a dense residual network (RDN) (Y. Zhang, Tian, et al., 2018) increased the depth of the network to more than 100. Then, residual channel attention was introduced into SR by RCAN (Y. Zhang, Li, et al., 2018). SR was also explored on the frequency domain (Zhou et al., 2019). Although these methods achieve impressive performance on SR tasks, the hallucinated details (El Helou, 2021; El Helou and Ssstrunk, 2022; Q. Liang et al., 2022) are often accompanied by unpleasant artifacts. Generative Adversarial Network (GAN) was used to enhance the visual quality of image SR networks. Inspired by relativistic GAN (Jolicoeur-Martineau, 2018), ESRGAN (X. Wang et al., 2018) was proposed and achieved better visual quality with more realistic image textures. Recently, the Transformer is introduced into image SR by SwinIR (J. Liang et al., 2021). Combining non-local operation and sparse representation, Non-Local Sparse Attention (NLSA, Mei et al., 2021) was implemented and achieved better performance on SR.

However, most existing SR networks are trained and evaluated on synthetic datasets such as Div2K (Agustsson and Timofte, 2017), Set14 (Zeyde et al., 2010) and B100 (Martin et al., 2001). In those datasets, the HR images are high-quality natural images, and the LR counterparts are generated with predefined downsample kernels. The degradation model in this setting is simpler than the one in real-world scenarios, which leads to a severe performance drop when these methods are evaluated on real-world images (Gu et al., 2019; Shocher et al., 2018; L. Wang, Wang, Dong, et al., 2021). To solve such problem, some real-world SR dataset are collected such as RealSR (Cai, Gu, et al., 2019; Cai, Zeng, et al., 2019), SR-RAW (X. Zhang et al., 2019), W2S (Zhou et al., 2020) and BurstSR (Bhat et al., 2021). BSRNet and BSRGAN (K. Zhang et al., 2021) were proposed leveraging a more complex but practical degradation model considering randomly shuffled blur, downsampling, and noise degradation. Combining an unsupervised degradation representation learning scheme and degradation aware block, DASR (L. Wang, Wang, Dong, et al., 2021) achieved better performance on blind SR task.

Zero-shot learning was introduced in SR to adapt networks to the new degradation model quickly. Researchers have found that adaptive networks achieved better performance, especially for unseen images (Park et al., 2020). ZSSR (Shocher et al., 2018) was proposed by training a small network at test time from scratch. The training samples of ZSSR were extracted and generated only from the given input image. Inspired by model agnostic meta-learning (MAML, Finn et al., 2017), MLSR (Park et al., 2020) was proposed and effectively handled unknown SR kernels. By finding a generic initial parameter suitable for internal learning, MZSR (Soh et al., 2020) yields better results with less gradient update.

2.3 Recent advances in image super-resolution dataset

Recently, some researchers found that using RAW data could achieve better performance on real-world SR tasks (X. Zhang et al., 2019). Therefore, some latest real-world SR datasets provide not only RGB data but also RAW data of LR and HR image pairs (Bhat et al., 2021; X. Zhang et al., 2019). On the other hand, multi-frame super-resolution (MFSR) (Bhat et al., 2021; Dudhane et al., 2021; Lecouat et al., 2021) usually yield better results than SISR. The input of the MFSR task is a sequence of LR images captured under the burst model. As different burst frames may contain sub-pixel information, this would improve the performance of SR methods. All premonitions methods are designed for fixed scale factors, making SR for arbitrary scale factors become an emerging task. Leveraging meta-learning, Meta-SR (Hu et al., 2019) was the first SR method for arbitrary scale factors. Then ArbSR (L. Wang, Wang, Lin, et al., 2021) was proposed by leveraging scale-aware feature adaption blocks and a scale-aware upsampling layer.

2.4 Summary

This chapter briefly reviews the development of drone-based computer vision research and image super-resolution. On the one hand, most existing drone-based vision datasets are designed for object detection and related tasks. To the best of our knowledge, none has proposed a drone vision dataset for the image SR task. On the other hand, the performance of existing SR networks is susceptible to the dataset, specifically, the degradation model between LR and HR images. Therefore, it is significant to propose the first drone vision dataset for image SR.

3 Data acquisition

This chapter introduces the detailed procedures to acquire our drone vision dataset for super-resolution (DroneSR). We first introduce the platform used in this project in Section 3.1. Then we explore the effects of different camera settings on captured images and our choice in Section 3.2 and Section 3.3. Finally, we summarize the whole data acquisition procedure in Section 3.7.

3.1 Platform

The platform consists of three parts: the drone itself, the cameras mounted on the drone, and the mobile application to control the drone and cameras.

3.1.1 Drone

We use DJI Mavic 3 drone (see Figure 3.1 for the appearance of the drone) for data acquisition. The drone has 3-axis gimbals to stabilize cameras. The control tilt range of cameras is -90° to $+35^\circ$. In this project, we only focus on the bird-view, which means the camera shoots on the top of objects, so the tilt angle is set to be -90° throughout the data acquisition process.

The drone utilizes the GNSS (GPS+Galileo+BeiDou), a vision system, and an infrared sensing system to locate and stabilize itself. When the GNSS signal is strong, the drone uses GNSS, and this mode's vertical hovering accuracy range is $\pm 0.5m$. On the other hand, if the GNSS signal is weak but the environmental conditions are sufficient, the drone switches to the vision system, and the accuracy range under this situation is $\pm 0.1m$.

3.1.2 Cameras

DJI Mavic 3 is equipped with two cameras: one primary camera is a 4/3-in CMOS sensor Hasselblad L2D-20c camera (referred to hereinafter as "Hasselblad camera"); the other is a 1/2-in CMOS sensor Tele camera (referred to hereinafter as "Tele camera"). Some specifications of



Figure 3.1: DJI Mavic 3 drone.

	Hasselblad camera	Tele camera
Sensor	4/3-in CMOS	1/2-in CMOS
Lens FOV	84°	15°
Lens Format Equivalent	24mm	162mm
Lens Aperture	$f/2.8 \sim f/11$	$f/4.4$
Lens Shooting Range	1m ~ ∞	3m ~ ∞
Electronic Shutter Speed	1/8000s ~ 8s	1/8000s ~ 2s
Max Image Size	5280 × 3956	4000 × 3000

Table 3.1: Specifications of cameras.

the two cameras are listed in Table 3.1.

The Tele camera has a larger focal length, so the image captured by the Tele camera can be considered as an optical zoom version of the one from the Hasselblad camera at the same position. Therefore, we choose the image from the Tele camera as our HR ground-truth and the image from the Hasselblad camera as our LR image to collect one LR and HR image pair for our dataset.

3.1.3 DJI Fly App

DJI Fly is a mobile application provided by the DJI company. Through this application, we can connect our mobile phones with the drone and display the real-time view captured by the camera. In addition, we can set camera parameters in DJI Fly. The available options are listed in Table 3.2^I.

^IThe latest drone firmware allows us to use burst mode on the Tele camera and acquire RAW data from the Tele camera. However, those functions are not provided at the beginning of the project.

Parameters	Options (Hasselblad camera)	Options (Tele camera)
ISO	100, 200, 400, 800, 1600, 3200, 6400	100 - 6400 (auto)
Shutter	1/8000, 1/6400, 1/5000, 1/4000, 1/3200, 1/2500, 1/2000, 1/1600, 1/1250, 1/1000, 1/800, 1/640, 1/500, 1/400, 1/320, 1/240, 1/200, 1/160, 1/120, 1/100, 1/80, 1/60, 1/50, 1/40, 1/30, 1/25, 1/20, 1/15, 1/12.5, 1/10, 1/8, 1/6.25, 1/5, 1/4, 1/3, 1/2.5, 1/2, 1/1.67, 1/1.25, 1", 1.3", 1.6", 2", 2.5", 3.2", 4", 5", 6", 8"	1/8000 - 2 (auto)
F-number	11.0, 10.0, 9.0, 8.0, 7.1, 6.3, 5.6, 5.0, 4.5, 4.0, 3.5, 3.2, 2.8	4.4
Size	<u>4:3</u> , 16:9	<u>4:3</u>
Focus Mode	MF(manual focus), <u>AF</u> (autofocus)	ME, <u>AF</u>
Burst Number	1, 3, 5, <u>7</u>	<u>1</u> , 3, 5, 7
Format	JPG, RAW, <u>JPG+RAW</u>	JPG, RAW, <u>JPG+RAW</u>
Anti-Flicker	off, <u>auto</u> , 50Hz, 60Hz	
Peaking Level	<u>off</u> , low, normal, high	
White Balance	<u>auto</u> , manual(2000k-10000k)	
Explore mode	off (only use Hasselblad camera), on (above X7, only use Tele camera)	

Table 3.2: Camera options of DJI Mavic 3 drone in DJI Fly App. The underlined options are chosen for data acquisition.

3.2 Manual camera settings

Camera settings are essential for data acquisition. The DJI Fly App provides two modes for us. One is manual mode, and we can change the f-number, ISO, and shutter time of the Hasselblad camera in this mode. The other is auto mode, where we can only choose exposure value (EV). We start with manual mode, test each parameter one by one and try to find the best setting for data acquisition.

3.2.1 F-number

In an optical system, the f-number (F) is defined as the ratio of the system's focal length to the diameter of the entrance pupil:

$$F = \frac{f}{D} \quad (3.1)$$

where f is the focal length, and D is the diameter of the entrance pupil (effective aperture).

The depth of field (DoF) defines the focused area within the distance between blurred near-

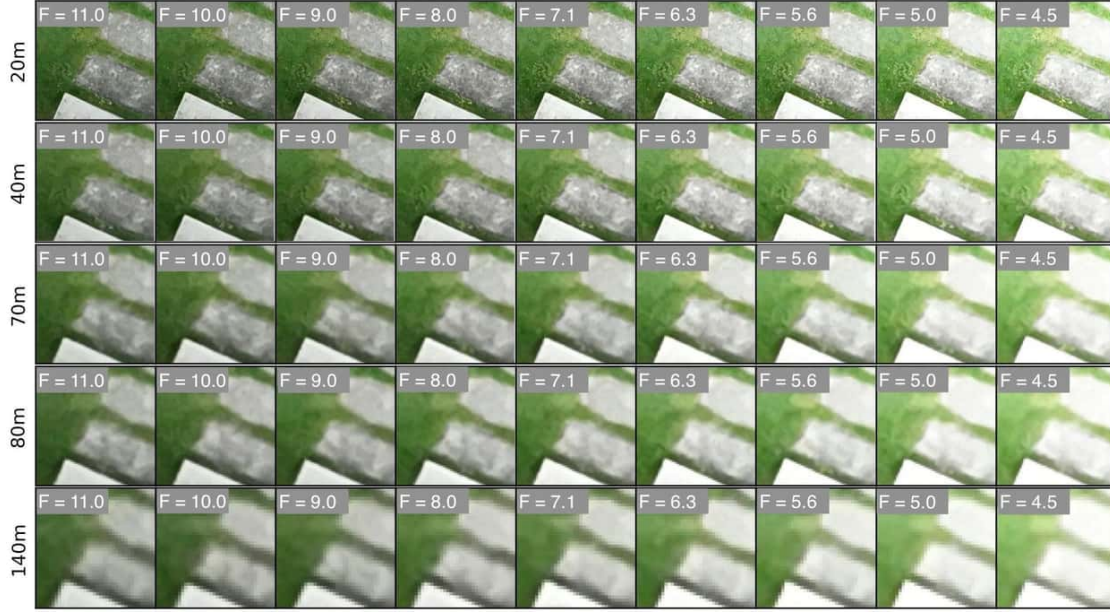


Figure 3.2: Example patches captured at different relative altitude and different f-number. All of the images were captured with 1/400s shutter time and 1600 ISO. The text on the left shows the relative altitude.

field and far-field objects. The approximate DoF can be given by:

$$DoF \approx \frac{2h^2Fc}{f^2} \quad (3.2)$$

where c is the circle of confusion, and h is the distance to the subject (i.e., relative altitude between the drone and ground). Object outside DoF suffers from blur. During the data acquisition process, we obtain images of different resolutions using two cameras of different focal lengths. To build a perfect LP and HR image pair, it would be ideal if we made DoF identical, but it is not practical (X. Zhang et al., 2019). Besides, our Tele camera has a fixed f-number (4.4, see Table 3.1), and we can not change the settings of the Tele camera.

To eliminate the influence caused by the DoF mismatch, SR-RAW (X. Zhang et al., 2019) chose a small aperture size (i.e., large f-number) for all images in the dataset. Since the DoF is related to relative altitude and f-number, we collect a small dataset to show the effect of f-number and relative altitude on captured image (see Figure 3.2). In addition, we crop small patches from the original images to show the effects more clearly. As we can see from Figure 3.2, the images suffer from more blur as the f-number decreases. However, since the image resolution decrease as relative altitude increase, it is hard to observe the same phenomenon on high-altitude images. As the f-number decreases, we observe the brightness of captured image increase, and it tends to overexposure because aperture size increases and more light comes into the lens.

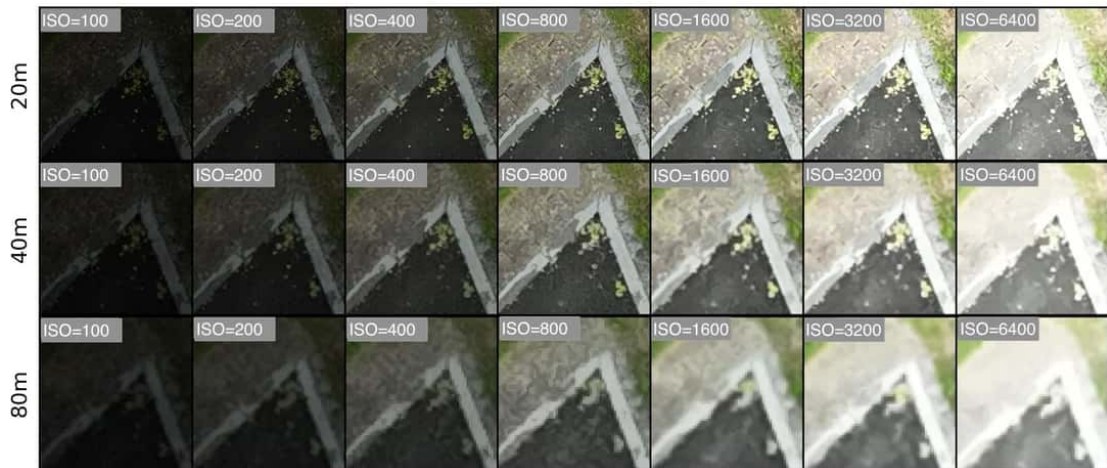


Figure 3.3: Example patches captured at different relative altitudes and different ISOs. All of the images were captured with 1/500s shutter time and 11.0 f-number. The text on the left shows the relative altitude.

3.2.2 ISO

To achieve proper exposure with a large f-number, we could adjust ISO. Increasing ISO could make the captured photos appear brighter. However, one side effect of larger ISO is that it brings more noise. We also collected a small dataset to show the effect of ISO and relative altitude on captured images (see Figure 3.3). We can find that as the ISO increase, more noise is introduced, and the brighter the images appear.

3.2.3 Shutter

Another setting that can be used to adjust the exposure of the captured image is shutter time. The shutter time is defined as the length of time that the camera's sensor is exposed to light when taking a photo. The longer the shutter time, the more light will come into the camera, and the brighter image will appear. However, a longer shutter time leads to a more severe blur due to the drone's vibration. We collected a small dataset to show the effect of shutter time and relative altitude on captured images (see Figure 3.4). The results prove that longer shutter time leads to brighter images, thus overexposure and more severe blur.

3.2.4 Summary of manual mode

The exposure is affected by f-number, shutter speed, and ISO. To minimize the DoF difference and blur, we could choose a large f-number. However, a large f-number leads to underexposure. We could increase shutter time and ISO to achieve proper exposure, leading to higher noise or more severe blur. Therefore, it's not practical to manually set all camera parameters at each sense and each altitude.

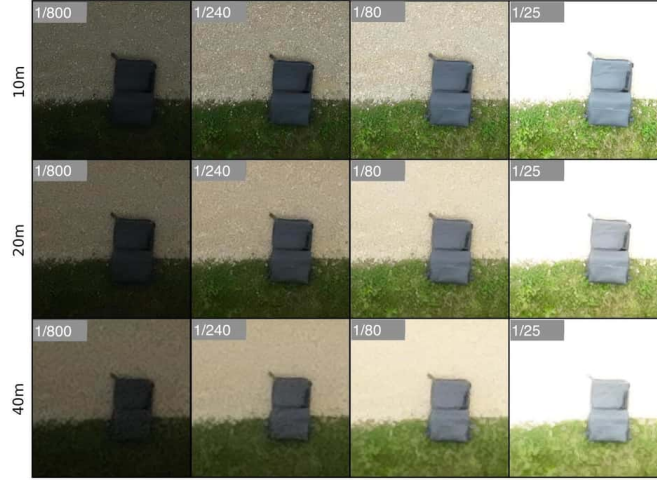


Figure 3.4: Example patches captured at different relative altitudes and different shutter times. All of the images were captured with 11.0 f-number and 400 ISO. The text on the left shows the relative altitude, and the text in the patches indicates the shutter time (in seconds).

On the other hand, we need an optical zoom-in image from the Tele camera as the HR ground-truth in our LR and HR image pair. However, we can only choose the auto mode when using the Tele camera. Therefore, we decided on auto mode for both cameras to minimize the brightness difference between LR and HR images.

3.3 Auto camera settings

Besides manual mode, the DJI Fly App also provides an auto mode. We can adjust the exposure value (EV) until the image is exposed correctly. In auto mode, when changing EV, the camera will automatically change its shutter time, f-number, and ISO to fit the chosen exposure value. We can use auto mode for both Hasselblad and Tele cameras. We chose the same EV for both cameras. Furthermore, we use the same EV when capturing images for all altitudes. Some examples are shown in Figure 3.5.

3.4 Compare lower altitude and optical zoom

Besides using optical zoom to generate LR and HR image pairs, we can collect LR and HR image pairs by taking photos at different altitudes. For example, images taken at lower altitudes can be regarded as HR counterparts of images taken at higher altitudes. We try various strategies to generate the HR and LR image pairs, showing the resulting HR patches in Figure 3.6. The first row shows patches of HR images captured at lower altitudes, and the second row shows patches of HR images captured using optical zoom. We can obviously find both methods yield good HR images. However, the vertical hovering accuracy of the drone is $\pm 0.5m$, which leads to the scale factor varying a lot if we choose a lower altitude image as our HR counterpart. In

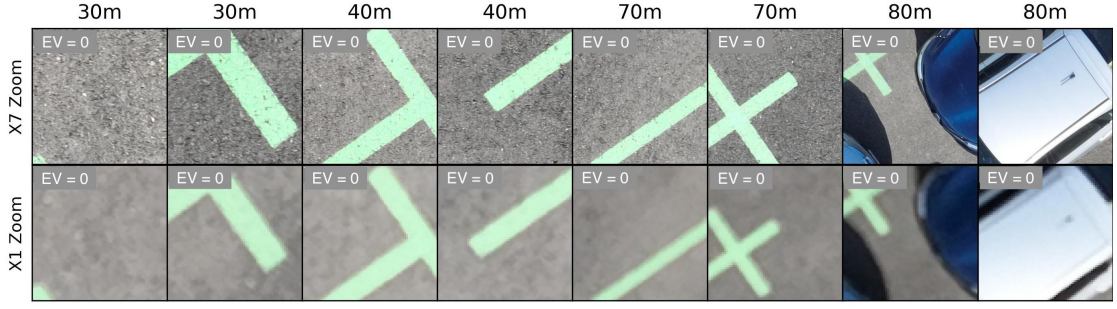


Figure 3.5: Examples of patches captured by different cameras. The Tele camera takes the top row, and the Hasselblad camera takes the bottom row. The text above each column shows the relative altitude of the drone where the pictures were captured.



Figure 3.6: Examples of lower altitude and optical zoom images. Images in the upper row are obtained from lower altitudes (10m or 20m) by the Hasselblad camera; images in the bottom row are obtained from higher altitudes (70m or 140m) by Tele camera (optical zoom).

addition, some challenges, such as perspective distortion, make the further alignment step very complex if we use a lower altitude image. Finally, we choose images captured by Tele camera at the same position as our HR ground-truth. We still collect LR and HR image pairs at different altitudes per scene in case later researchers want to use lower altitude images as HR for the arbitrary scale factor task.

3.5 Comparison between burst frames

MFSR has been proven to yield better performance than SISR (Bhat et al., 2021). We use the burst mode of the Hasselblad camera and take some burst sequence examples. Then we calculate the PSNR and SSIM (Z. Wang et al., 2004) between each burst frame. The results are shown in Figure 3.7. Although each burst frame looks very similar, the numerical results show that they are not identical, indicating sub-pixel information may be contained in the sequence. We don't use the burst sequence in this project, but to benefit the later researchers, we choose burst mode when capturing LR images during data acquisition.

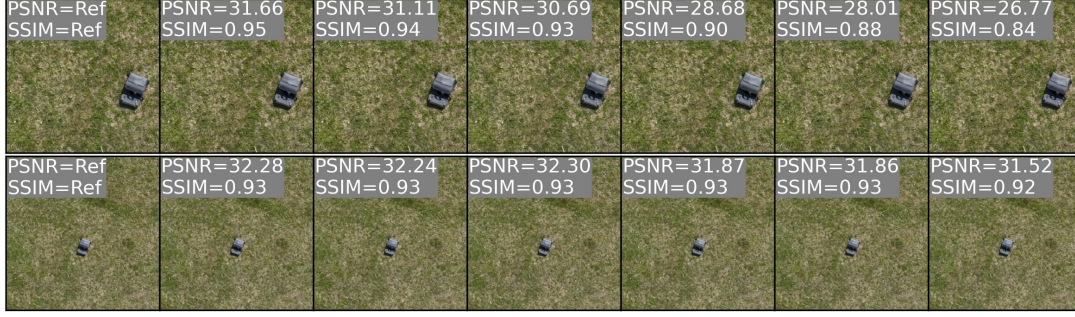


Figure 3.7: Examples of the burst sequence. The numerical results indicate the differences between burst frames.

3.6 Scene selection

To increase the diversity of our dataset, we need to select as many different scenes as possible and tend to capture images in more flat areas and static scenes to eliminate the mismatch between LR and HR image pairs. For the drone's safety, we also need to collect data where the drone can receive a strong or moderately strong GNSS signal. Due to Swiss drone regulations, we are not allowed to fly the drone close to a group of people.

3.7 Summary

In conclusion, we choose the image from the Tele camera as our HR ground-truth and the image from the Hasselblad camera as our LR image to collect one image pair for our dataset, and we chose auto mode for both cameras with the same EV. In this way, we collect image pairs at different altitudes per scene and keep EV the same among all altitudes. The final data acquisition procedures are listed below:

1. Take off the drone from some static and flat place with a strong GNSS signal;
2. Raise the drone to 10m above the starting point;
3. Zoom in X7 (use Tele camera); adjust EV to capture a high-quality image; Save both JPEG and RAW format data;
4. Disable zoom in (use Hasselblad camera); turn on auto mode, keep the same EV as step 3); turn on burst mode, choose seven frame burst and capture seven frames;
5. Raise the drone to 20m, 30m, 50m, 40m, 70m, 80m, 100m, 120m, and 140m above the starting point. At each altitude, repeat step 3) and step 4), keep EV the same through all altitudes.

Finally, following the setting in BurstSR (Bhat et al., 2021), we capture 200 scenes in total, which are split into train, validation, and test sets consisting of 160, 20, and 20 scenes, respectively.

4 Data pre-processing

This chapter covers the pre-processing steps on the LR and HR image pairs directly captured by the cameras. We first find matched field of view (FOV) in LR images in Section 4.1. Then, we apply local alignment on patches of image pairs to eliminate the misalignment problem in Section 4.2. Finally, we find the RGB colors of the HR image and LR image are different. To solve this problem, we develop a color correction method in Section 4.3.

4.1 Field of view matching

Since the images captured by the Hasselblad camera and the Tele camera have different fields of view (FOV), we first crop out the matched FOV from each Hasselblad camera image in the burst sequence. For real-world image FOV matching, Cai, Zeng, et al., 2019; X. Zhang et al., 2019 simply cropped around the center of the LR images because they used only one camera to acquire HR and LR pairs and adjust the focal lengths to achieve optical zoom. They fixed the camera on a tripod, making the center of the HR and LR pair almost not change. However, manually zooming the camera to adjust focal lengths might cause slight camera movement. For alignment, X. Zhang et al., 2019 applied a Euclidean motion model that allows image rotation and translation via enhanced correlation coefficient (Evangelidis and Psarakis, 2008). They firstly calculated the alignment between HR and LR RGB images and then apply the alignment to RAW images. Cai, Zeng, et al., 2019 avoided this problem by using a Bluetooth remote controller. However, those methods do not work well in our dataset as we use two cameras to capture HR and LR images separately, and the vibration of a drone in the air is more severe than human hands and can not be avoided.

Bhat et al., 2021 also used two cameras to capture HR and LR images separately. One phone camera was used to capture LR, and one digital single-lens reflex (DSLR) camera was used to capture HR. The DSLR camera was also fixed on a tripod, and they held the phone camera by hand just above the DSLR to minimize misalignment. For FOV matching, they estimated the homography between the first image in the LR burst sequence and HR image using SIFT (Lowe, 1999) and RANSAC (Fischler and Bolles, 1981) (see Figure 4.1 for an example). We use

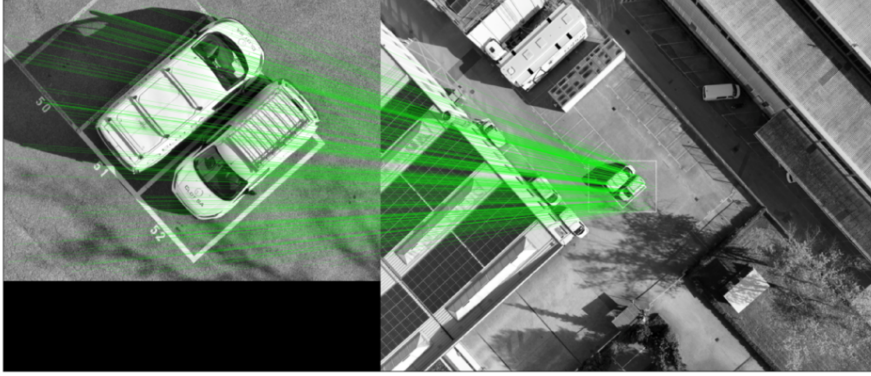


Figure 4.1: Example of using feature matching (SIFT (Lowe, 1999) and RANSAC (Fischler and Bolles, 1981)) and homography to find FOV in LR. The image on the left is our HR image, and the image on the right is our LR image. The white rectangle in the LR is matched FOV.

the same procedure to find matched FOV in our LR images. However, in our case, the drone vibrates not only horizontally but also vertically, which leads to the size of FOV on the LR image also varying (see the second row in Figure 4.2 for some examples). Although the variation is only a few pixels, this will complicate the rest of the data preprocessing steps and lead to a varying scale factor. We resize the FOV into a fixed size (720×540). Since the size of most matched FOV is around this value. The full size of our HR image is 4000×3000 . Therefore, the scale factor of our DroneSR dataset is $50/9$. For this resize step, we try different interpolation methods (see the third row to the fifth row in Figure 4.2 for more details). We calculate the normalized cross correlation between resized LR images and downsampled HR images and find the results are very similar among all interpolation methods. We think this is because the new size of the LR image is very close to the original one, with only a few pixels difference. So different interpolation gets very similar results. Finally, we choose the nearest-neighbor interpolation method in this step.

4.2 Local alignment

Like BurstSR (Bhat et al., 2021), we extract patches from the LR images in a sliding window manner. To avoid any overlap among patches, we extract 180×180 patches from LR images with a stride of 180 pixels. For each patch, we again estimate homography between the LR patch and the corresponding region in the HR image to perform a local alignment. Finally, we filter out HR and LR pairs with a normalized cross-correlation of less than 0.9 (Bhat et al., 2021). Some resulted LR patches are shown in Figure 4.3 row (b), and the corresponding downsampled HR patches are shown in Figure 4.3 row (a).



Figure 4.2: FOV matching examples: the HR image is the full image captured by the Tele camera of size (4000 × 3000s). The second row shows the matched FOV directly obtained from feature matching and homography. The rest row shows the resized FOV after different interpolation methods. The size of matched FOV is shown in the top-left corner of the image. Finally, the normalized cross-correlation is calculated between matched FOV and downsampled HR images.

4.3 Color correction

Although we chose the same EV (EV=0) for both Hasselblad and Tele cameras, we still observe the color and luminance difference between HR and LR pairs (see Fig 4.3 row (a) and (b) for some examples). However, pixel-wise registration is necessary for our dataset. We need to eliminate the mismatched color. To obtain accurate image pair registration, we implemented the pixel-wise color transfer algorithm in RealSR (Cai, Zeng, et al., 2019), which simultaneously considers luminance adjustment. Besides this method, we also try histogram matching^I between HR and LR pairs, and apply white balance correction (Afifi et al., 2019) on HR and LR pairs. We find color transfer and histogram matching are more efficient. To compare the performance of different color correction methods, we first calculate the PSNR and SSIM between downsampled HR and LR in a real-world image dataset RealSR (Cai, Gu, et al., 2019; Cai, Zeng, et al., 2019) (see Table. 4.1). Then we try different color correction methods separately and also combine them in a different order. We evaluate those methods on our full dataset, the numerical results are shown in Table 4.2 and some samples are shown in Figure

^Ihttps://scikit-image.org/docs/dev/auto_examples/color_exposure/plot_histogram_matching.html#sphx-gl-r-auto-examples-color-exposure-plot-histogram-matching-py

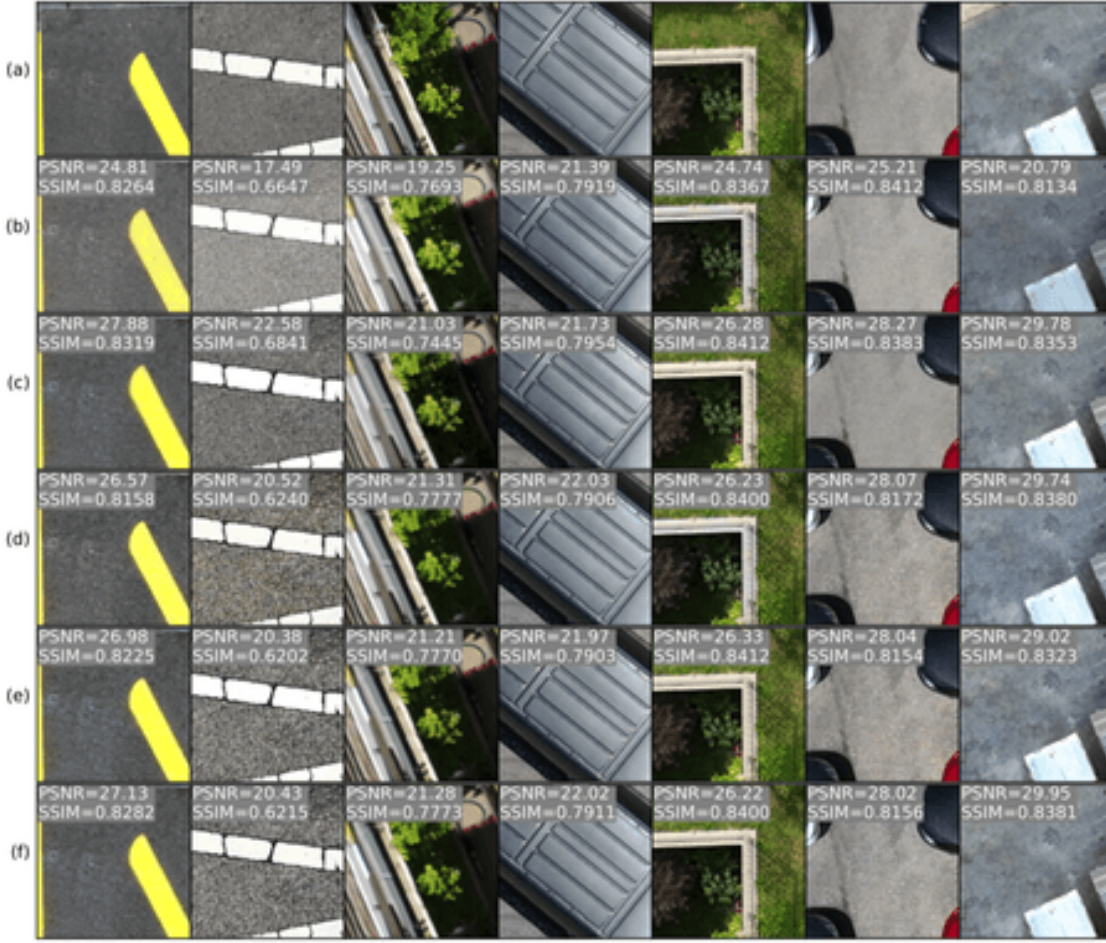


Figure 4.3: Examples to show the performance of methods for the color mismatch problem. (a): Bicubic downsampled HR images; (b): LR images; (c): Histogram matching; (d): Color transform (Cai, Zeng, et al., 2019); (e): Histogram matching+Color transform; (f): Color transform+Histogram matching. All results are calculated on the Y channel in the transformed YCbCr space.

4.3 row (c)-(f). According to Table 4.2, we choose color transfer and histogram matching in sequential as it achieves the best performance.

4.4 Misalignment analysis

Misalignment is unavoidable during data acquisition and is hard to be eliminated by the pre-processing step. By comparing the results in Table 4.1 and Table 4.2, our dataset suffers more misalignment than other real-world SR datasets, which is reasonable. Since we capture data with different focal lengths, misalignment is inherently caused by perspective changes. Furthermore, we did not capture the HR and LR images synchronously. There is no absolute flat ground. Thus any vibration of the drone would lead to the movement of the perspective

Scale factor	x2	x3	x4
PSNR/SSIM	32.25/0.9318	30.20/0.9105	29.7484/0.9113

Table 4.1: PSNR/SSIM between LR images in the RealSR (Cai, Gu, et al., 2019; Cai, Zeng, et al., 2019) dataset and corresponding downsampled HR images. All results are calculated on the Y channel in the transformed YCbCr space.

Altitude (m)	10	20	30	40	50
Origin LR	20.12/0.7365	20.90/0.7588	21.17/0.7733	21.44/0.7890	21.60/0.7939
Histogram Matching (HM)	23.74/0.7598	24.59/0.7814	25.04/ 0.7959	25.35/ 0.8079	25.39/0.8109
Color Transfer (CT)	23.65/0.7601	24.52/0.7813	24.91/0.7950	25.17/0.8067	25.22/0.8102
HM + CT	23.80 /0.7599	24.63 /0.7809	25.06 /0.7949	25.36 /0.8071	25.42 /0.8103
CT + HM	23.77/ 0.7606	24.63 / 0.7814	25.06 /0.7954	25.36 /0.8075	25.42 /0.8107
Altitude (m)	70	80	100	120	140
Origin LR	21.52/0.8004	21.54/0.8025	21.67/0.8114	21.99/0.8233	22.14/0.8269
Histogram Matching (HM)	25.63/ 0.8176	25.66/ 0.8192	25.87/0.8287	26.03/ 0.8392	26.07/ 0.8420
Color Transfer (CT)	25.47/0.8169	25.50/0.8184	25.66/0.8276	25.79/0.8370	25.83/0.8401
HM + CT	25.67/0.8171	25.70/0.8185	25.92/0.8285	26.08/0.8386	26.12/0.8417
CT + HM	25.68 /0.8174	25.71 /0.8186	25.93 / 0.8290	26.09 /0.8387	26.13 / 0.8420

Table 4.2: PSNR/SSIM between LR patches with different color correction methods and corresponding downsampled HR patches in our dataset. All results are calculated on the Y channel in the transformed YCbCr space. The best results are in bold.

center, which leads to misalignment (Fig. 4.4b). Besides, it is hard to find static scenes. For example, the wind may cause a slight movement of vegetation (Fig. 4.4b). Furthermore, sharp details in the HR images cannot be perfectly aligned in the LR image (X. Zhang et al., 2019, Figure. 4.4c). The vibration of drones is much more severe than a tripod and human hands, which leads to more severe misalignment problems in our DroneSR dataset. This is inherently caused by the drone and scene and is unavoidable.

4.5 Summary

The images captured by the Hasselblad and Tele cameras have different FOVs. We first apply FOV matching on the LR image. Then, we use local alignment to eliminate the misalignment between LR and HR pairs and filter out patches with severe misalignment. After that, we notice the color mismatch between HR and LR pairs. Therefore, a color correction algorithm is developed. We visually check some resulted patches and find that misalignment still exists and can not be avoided in a real-world scenario. Due to the inherent property of our platform and scene, our DroneSR dataset suffers more severe misalignment than other real-world SR datasets collected by DSLR with a tripod. Finally, the statistics of the valid number of patches in each split of our dataset are shown in Figure 4.5. Our dataset can be regarded as a balanced dataset among all altitudes.

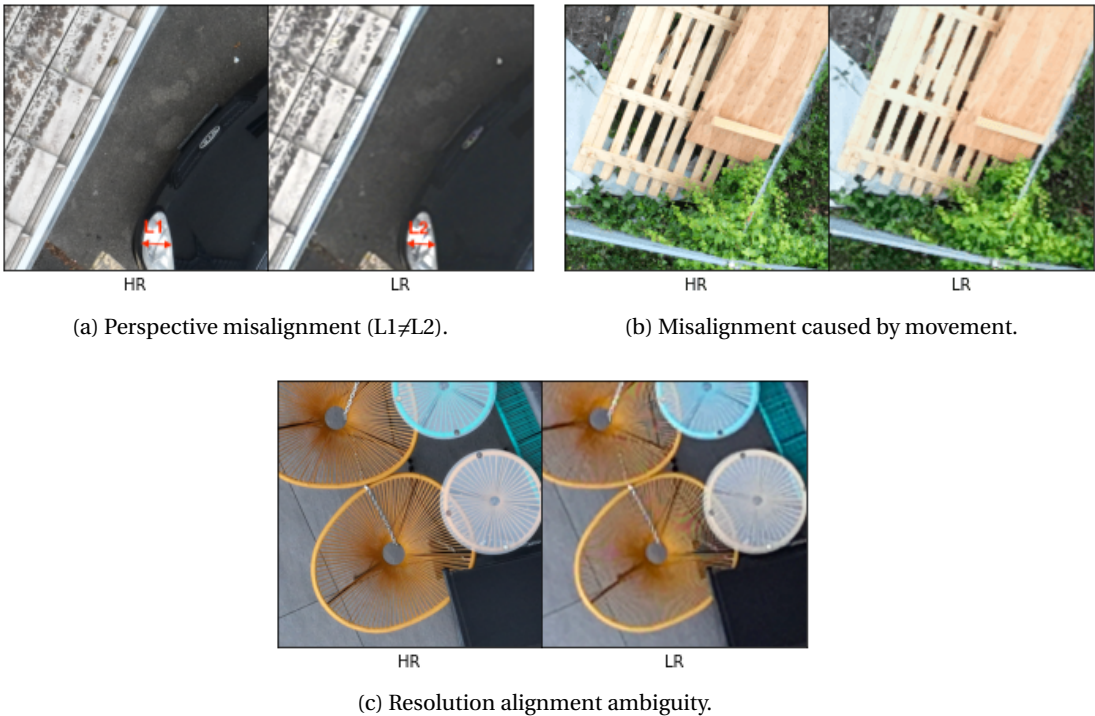


Figure 4.4: Examples of noticeable misalignment.

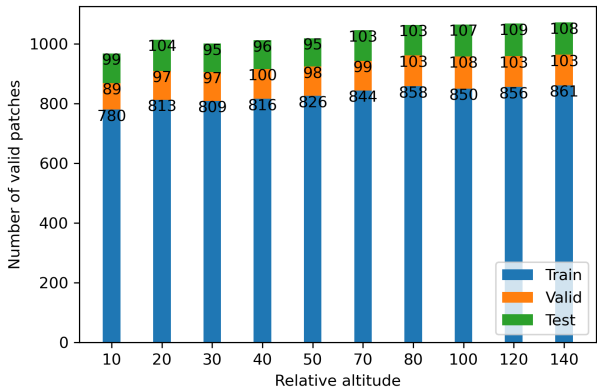


Figure 4.5: Statistics of our dataset.

5 Domain gap observation

This chapter explores the effects of different altitudes in our DroneSR dataset on SISR networks. We first introduce the degraded performance of pretrained SISR networks in a real-world dataset in Section 5.1. Then we evaluate the pretrained SR networks on our DroneSR datasets at different altitudes. Next, we fine-tune pretrained networks on our dataset. We propose two experimental setups to fine-tune and evaluate those SR networks separately in Section 5.3. Finally, we summarise and analyze our results in Section 5.4 for further research.

5.1 From synthetic downsampling to real-world degradation

Most of the existing learning-based SISR networks are trained and evaluated on synthetic dataset such as Div2K (Agustsson and Timofte, 2017), Flickr2K (Lim et al., 2017; Timofte et al., 2017), WED (Ma et al., 2016), FFHQ (Karras et al., 2019), Set5 (Bevilacqua et al., 2012), Set14 (Zeyde et al., 2010), B100 (Martin et al., 2001) and Urban100 (Huang et al., 2015), where the LR images are generated by applying some simple and uniform degradation model (i.e., MATLAB bicubic downsampling) to HR images. However, the degradation model of real-world LR images is far more complicated. Many researchers (Cai, Zeng, et al., 2019) have found that SISR models trained on synthetic data did not perform well in practical scenarios. In Table 5.1, we evaluate some SOTA SISR networks (EDSR(Lim et al., 2017), RDN(Y. Zhang, Tian, et al., 2018), RCAN(Y. Zhang, Li, et al., 2018), ESRGAN(X. Wang et al., 2018) and DASR (L. Wang, Wang, Dong, et al., 2021)) on some public synthetic datasets (Div2K, Set5, Set14, B100, Urban100) and one real-world dataset called RealSR (Cai, Gu, et al., 2019; Cai, Zeng, et al., 2019). We downloaded the pretrained SISR networks provided by their authors with a fixed scale factor: $\times 4$. All networks were pretrained on Div2K datasets with bicubic downsampling, except that ESRGAN and DASR were pretrained on both Div2K and Flickr2K datasets, and a designed degradation model was used to generate the LR images for DASR. Following the setting in Y. Zhang, Tian, et al., 2018, we calculate the PSNR, SSIM Z. Wang et al., 2004, on the Y channel of the transformed YCbCr color space. Since the misalignment problem is more severe in our dataset, the pixel-wise PSNR assessment may not work effectively. We introduce LPIPS (R. Zhang et al., 2018) for image quality assessment. Note that LPIPS is used to measure perceptual

Method	Metric	Public (Bicubic downsampling)					Real image
		Div2K	Set5	Set14	B100	Urban100	RealSR
Bicubic	PSNR	28.24	28.62	26.00	26.07	23.23	27.28
	SSIM	0.9871	0.8264	0.8001	0.6731	0.9084	0.9066
	LPIPS	0.4018	0.3376	0.4181	0.4476	0.4037	0.4084
	GMSD	0.0997	0.0965	0.1175	0.1122	0.1478	0.1614
EDSR	PSNR	30.74	32.37	28.50	27.75	26.63	27.64
	SSIM	0.9951	0.9099	0.8655	0.7428	0.9670	0.9134
	LPIPS	0.3238	0.2391	0.3356	0.3743	0.2783	0.3953
	GMSD	0.0580	0.0414	0.0662	0.0761	0.0759	0.1535
RDN	PSNR	30.62	32.24	28.42	27.68	26.34	27.64
	SSIM	0.9950	0.9084	0.8633	0.7398	0.9641	0.9135
	LPIPS	0.3296	0.2430	0.3401	0.3788	0.2903	0.3953
	GMSD	0.0596	0.0418	0.0678	0.0774	0.0802	0.1535
RCAN	PSNR	30.73	32.52	28.57	27.77	26.72	27.65
	SSIM	0.9950	0.9113	0.8659	0.7438	0.9673	0.9135
	LPIPS	0.3235	0.2386	0.3350	0.3741	0.2749	0.3952
	GMSD	0.0582	0.0416	0.0659	0.0761	0.0756	0.1533
ESRGAN	PSNR	28.18	30.34	26.11	25.31	24.35	27.57
	SSIM	0.9901	0.8672	0.7958	0.6502	0.9458	0.9113
	LPIPS	0.2431	0.1953	0.2621	0.2882	0.2274	0.3969
	GMSD	0.0741	0.0522	0.0834	0.0947	0.0928	0.1551
DASR	PSNR	30.27	31.87	28.17	27.52	25.80	27.79
	SSIM	0.9944	0.9048	0.8599	0.7368	0.9591	0.9178
	LPIPS	0.3373	0.2455	0.3479	0.3838	0.3039	0.3880
	GMSD	0.0635	0.0443	0.0714	0.0791	0.0878	0.1478

Table 5.1: Evaluation results of SOTA SR networks on public synthetic and real-world SR datasets. All networks and datasets have a fixed scale factor of 4, We evaluate the results using PSNR, SSIM, LPIPS, and GMSD on the Y channel in the transformed YCbCr space.

quality, and a lower LPIPS value means the super-resolved image is more perceptually similar to the ground truth. Besides, we also add gradient-based assessment GMSD (Xue et al., 2013). The higher the GMSD score indicates a larger distortion range, and thus the lower the image perceptual quality.

We can obviously find that the performance of the leaning-based SISR model drops on a real-world dataset (ReaSR) if they are trained on synthetic generated HR-LR pairs. Since the degradation model is different among different datasets, we believe there is a domain gap between synthetic SR datasets and real-world SR datasets.

5.2 Effects of altitudes on pretrained SISR networks

In our DroneSR dataset, we capture LR and HR pairs at different altitudes, enabling us to evaluate SISR networks' performance at different altitudes. In Table 5.2 and Table 5.3, we evaluate some SOTA SISR networks (EDSR(Lim et al., 2017), RDN(Y. Zhang, Tian, et al., 2018), RCAN(Y. Zhang, Li, et al., 2018), ESRGAN(X. Wang et al., 2018), SwinIR(J. Liang et al., 2021), BSRNet(K. Zhang et al., 2021), NLSN (Mei et al., 2021) and DASR(L. Wang, Wang, Dong, et al., 2021)) on public synthetic datasets (Div2K, Set5, Set14, B100, Urban100) and our dataset at different altitudes. The LR images of public synthetic datasets are generated by MATLAB bicubic imresize method based on the scale factor of DroneSR ($\times 50/9$). Following the same procedures in previous section, we downloaded the pretrained SISR models the authors gave with a fixed scale factor: $\times 4$. With a designed degradation model, the BSRNet was pretrained on Div2K, Flickr2K, WED, and FFHQ datasets. SwinIR and NLSN were pretrained on Div2K datasets with bicubic downsampling. To fit our scale factor, we feed our LR images into SR networks, then upscale the outputs to the target size using bicubic interpolation. We also calculate the PSNR, SSIM (Z. Wang et al., 2004), LIPIS (R. Zhang et al., 2018) and GMSD (Xue et al., 2013) on the Y channel of the transformed YCbCr color space. The results are shown in Table 5.2 and Table 5.3.

As we can see from Table 5.2 and Table 5.3. The learning-based networks perform worse on our dataset and even worse than bicubic. We believe that this is caused by many factors. Firstly, the quality of the cameras on the drone is not as good as DSLR used in other real-world SR datasets, which leads to a more complicated degradation model. Secondly, the drone vibrates a lot, which leads to a more severe blur and a more complex degradation model. Thirdly, as mentioned in Section 4.4, the misalignment in the real-world SR dataset is unavoidable and more severe in our dataset. Finally, the color mismatch problem still exists in our dataset.

On the other hand, the performance of pretrained SOTA SR networks also varies among different altitudes. The content and texture viewed by the drone at different altitudes also vary, making each subset an individual domain, which is different from the train set of SR networks. More detailed analyses are given in Section 5.4.

5.3 Effects of altitudes on fine-tuned SISR networks

To further evaluate the performance of learning-based networks on our DroneSR dataset at various altitudes and in-depth analyze the domain gap among altitudes. We finetune a simple and fully convolutional network on our dataset. The network contains eight hidden layers, and each layer has 128 channels. We use ReLU activations on each layer. The input LR image is interpolated to the target size before being fed into the network. Following previous CNN-based SR methods (Kim et al., 2016a, 2016b), we only learn the residual between the interpolated LR and its HR counterpart. The detailed architecture of our CNN network is shown in Figure 5.1. We use L1 loss with ADAM (Kingma and Ba, 2014) optimizer. We first

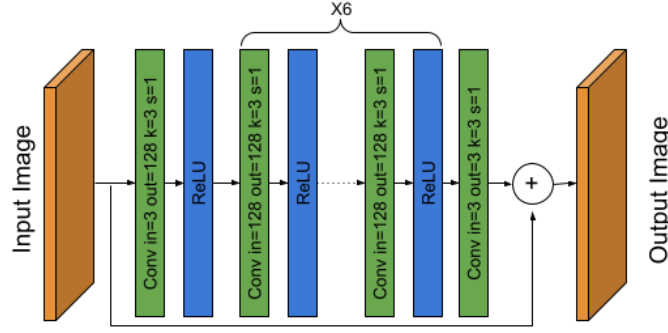


Figure 5.1: Detailed architecture of our simple CNN network.

pretrain the network on the public Div2K dataset with synthetic LR and HR pairs. We randomly crop the HR image into patches of size 300×300 with a batch size of 16 for training, and data augmentation is performed through random rotation and flipping. We start with a learning rate of 1×10^{-4} , train 1000 epochs in total, and half the learning rate every 200 epochs.

Then, we propose two setups to fine-tune the pretrained network:

Setup 1: we fine-tune the pretrained network on our DroneSR dataset with data of all altitudes. The initial learning rate is 1×10^{-5} . We fine-tune 100 epochs in total and half the learning rate every 20 epochs. The rest hyper-parameters are the same as for pretraining. **Setup 2:** we fine-tune the pretrained network on subsets of our DroneSR dataset at each altitude. The initial learning rate is also 1×10^{-5} . Since each subset contains far less data than the whole dataset, we fine-tune 500 epochs in total and half the learning rate every 100 epochs. The rest hyper-parameters are the same as for pretraining.

Finally, we evaluate the performance of those fine-tuned networks as well as the pretrained network at each altitude. Numerical results are shown in Table 5.4. we find that fine-tuning model at a specific altitude and then evaluating the model at the same altitude could yield better performance on PSNR. Furthermore, fine-tuning the model on the whole dataset with all altitudes achieves relatively better results than in situations where training altitude and evaluation altitude are largely mismatched, indicating domain gaps exist between subsets of different altitudes. We can also conclude that altitude affects the performance of SR models for drone vision, especially when the model is evaluated at different altitudes from the train set.

5.4 Analysis

As the drone flies higher, the captured image will lose more high-frequency details. To show this, we calculate the power spectrum density (PSD) of our test set images. We crop the center from higher altitudes images to keep the FOV the same among all altitudes. The averaged PSD among all scenes is shown in Figure 5.2. It is evident that images captured at lower altitudes

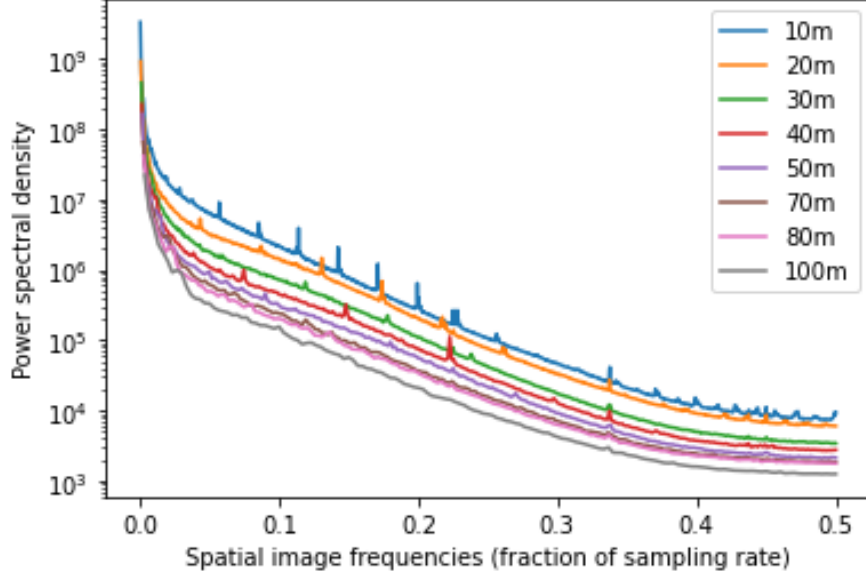


Figure 5.2: Image frequency content (image PSD) of different altitude.

contain more high-frequency details. This further proves the domain gap between subsets among different altitudes. El Helou et al., 2020 have found that frequency domain changes would affect SR networks' performance. Therefore, the performance of SR networks varies at different altitudes.

We also observe the mismatch between HR and SR images by calculating the absolute difference between the bicubic upsampled image and HR image; see Figure A.1 for more examples. As the drone goes up, the mismatch between HR and SR tends to appear in areas with more details. We also find that bicubic upsampling performs well at edges, which indicates our HR may suffer from severe blur due to the vibration of the drone and explains why bicubic upsampling surpasses pretrained SR networks on our dataset.

In the fine-tuning experiments, we observe that fine-tuning on 10m performs best at lower ($\leq 40m$) altitudes in the PSNR, and fine-tuning on 140m performs best at higher altitudes. We illustrate some visual examples of fine-tuning in Section A.2. We have found the captured HR images at lower altitudes contain more high-frequency information, and these parts affect the final results more at lower altitudes. Accordingly, the data of 10m includes the most high-frequency details, and thus network fine-tuned on this set tends to perform better on high-frequency information. Therefore, it serves the best at lower altitudes. On the other hand, the images captured at 140m cover the most expansive area, thus increasing the diversity of the training set. Besides, the HR images suffer less blur from the drone's vibration due to the more considerable distance between the camera and the object. Therefore, the SR network is better trained on a subset of 140m. Furthermore, the network finetuned on the whole dataset is trained on more data with all altitudes. Hence, it performs well among all altitudes. We also illustrate more test samples of fine-tuned models at varying altitudes in Section A.2.

5.5 Summary

In this chapter, we explore the performance of the existing SR methods on real-world SR datasets. We observe the models trained on synthetic datasets perform less effectively in real-world scenarios. We also find that the performance of those models varies at different altitudes in our DroneSR dataset. Furthermore, we also see the performance of the SR model drops when the model is evaluated at different altitudes from the train set. This motivates us to build a robust SR model for drone vision at varying altitudes.

Method	Metric	Public					Our		
		Div2K	Set5	Set14	B100	Urban100	10m	20m	30m
Bicubic	PSNR	26.56	26.37	24.30	24.62	21.82	23.12	22.69	23.39
	SSIM	0.9593	0.7504	0.7065	0.6013	0.7722	0.7089	0.6836	0.6992
	LPIPS	0.4731	0.4149	0.4963	0.5281	0.4851	0.5769	0.5959	0.5836
	GMSD	0.1435	0.1469	0.1641	0.1565	0.1979	0.1836	0.1983	0.1996
EDSR	PSNR	28.27	28.91	26.07	25.80	23.76	22.95	22.52	23.27
	SSIM	0.9796	0.8581	0.7870	0.6657	0.8793	0.7099	0.6860	0.7027
	LPIPS	0.3911	0.2959	0.4065	0.4498	0.3530	0.5435	0.5605	0.5525
	GMSD	0.1031	0.0889	0.1181	0.1229	0.1391	0.1880	0.2013	0.2014
RDN	PSNR	28.20	28.73	26.06	25.75	23.62	22.96	22.53	23.28
	SSIM	0.9791	0.8540	0.7841	0.6626	0.8732	0.7100	0.6861	0.7029
	LPIPS	0.3979	0.3010	0.4118	0.4556	0.3679	0.5455	0.5626	0.5540
	GMSD	0.1050	0.0922	0.1195	0.1246	0.1442	0.1874	0.2008	0.2009
RCAN	PSNR	28.27	28.78	26.11	25.81	23.82	22.93	22.51	23.26
	SSIM	0.9795	0.8575	0.7867	0.6668	0.8814	0.7097	0.6858	0.7026
	LPIPS	0.3900	0.2971	0.4055	0.4488	0.3472	0.5430	0.5604	0.5520
	GMSD	0.1031	0.0882	0.1178	0.1229	0.1373	0.1889	0.2021	0.2022
ESRGAN	PSNR	26.35	26.66	24.53	24.01	22.25	22.78	22.37	23.13
	SSIM	0.9666	0.7976	0.7186	0.5890	0.8372	0.7070	0.6833	0.7000
	LPIPS	0.3220	0.2700	0.3445	0.3637	0.3007	0.5316	0.5637	0.5569
	GMSD	0.1155	0.1093	0.1289	0.1333	0.1476	0.1884	0.2015	0.2014
BSRNet	PSNR	27.22	27.17	24.99	25.16	22.75	22.38	22.09	22.83
	SSIM	0.9651	0.7924	0.7309	0.6285	0.8269	0.7021	0.6818	0.6992
	LPIPS	0.4573	0.3756	0.4761	0.5175	0.4387	0.5471	0.5584	0.5492
	GMSD	0.1329	0.1259	0.1568	0.1531	0.1816	0.1935	0.2024	0.2034
SwinIR	PSNR	28.45	28.79	26.10	25.88	24.09	22.91	22.47	23.22
	SSIM	0.9809	0.8630	0.7930	0.6727	0.8946	0.7095	0.6852	0.7019
	LPIPS	0.3816	0.2952	0.3996	0.4409	0.3335	0.5451	0.5610	0.5530
	GMSD	0.0989	0.0879	0.1164	0.1202	0.1291	0.1902	0.2035	0.2034
NLSN	PSNR	28.31	28.91	26.15	25.86	24.00	22.95	22.52	23.27
	SSIM	0.9796	0.8607	0.7891	0.6689	0.8862	0.7099	0.6859	0.7027
	LPIPS	0.3893	0.2917	0.4037	0.4433	0.3418	0.5440	0.5605	0.5518
	GMSD	0.1026	0.0868	0.1164	0.1210	0.1330	0.1887	0.2020	0.2021
DASR	PSNR	27.97	28.25	25.83	25.64	23.36	23.03	22.60	23.32
	SSIM	0.9775	0.8447	0.7769	0.6590	0.8633	0.7106	0.6866	0.7030
	LPIPS	0.4067	0.3100	0.4218	0.4614	0.3864	0.5484	0.5658	0.5561
	GMSD	0.1087	0.0972	0.1232	0.1259	0.1503	0.1871	0.2007	0.2012

Table 5.2: Evaluation results of SOTA SR networks on public and our dataset at different altitudes. Our dataset has a scale factor of 50/9, and all public datasets are downsampled according to this scale factor using the MATLAB bicubic kernel function. We upscale the networks' output to fit our scale factor for the networks that are not pre-trained on our scale factor. We evaluate the performance using PSNR, SSIM, LPIPS, and GMSD on the Y channel in the transformed YCbCr space.

Method	Metric	Our						
		40m	50m	70m	80m	100m	120m	140m
Bicubic	PSNR	24.25	24.41	24.14	24.16	24.27	24.34	24.41
	SSIM	0.7325	0.7418	0.7456	0.7518	0.7655	0.7668	0.7724
	LPIPS	0.5694	0.5727	0.5633	0.5584	0.5572	0.5597	0.5581
	GMSD	0.1903	0.1932	0.1920	0.1909	0.1875	0.1883	0.1872
EDSR	PSNR	24.07	24.29	23.98	23.99	24.11	24.17	24.24
	SSIM	0.7346	0.7455	0.7481	0.7542	0.7689	0.7700	0.7758
	LPIPS	0.5429	0.5472	0.5388	0.5343	0.5336	0.5364	0.5367
	GMSD	0.1927	0.1945	0.1947	0.1935	0.1895	0.1902	0.1896
RDN	PSNR	24.09	24.30	24.00	24.00	24.12	24.18	24.25
	SSIM	0.7348	0.7456	0.7484	0.7544	0.7690	0.7702	0.7760
	LPIPS	0.5438	0.5481	0.5395	0.5351	0.5346	0.5372	0.5371
	GMSD	0.1924	0.1944	0.1944	0.1933	0.1894	0.1901	0.1893
RCAN	PSNR	24.07	24.28	23.98	23.97	24.10	24.16	24.23
	SSIM	0.7345	0.7454	0.7482	0.7541	0.7687	0.7702	0.7758
	LPIPS	0.5423	0.5466	0.5385	0.5347	0.5336	0.5367	0.5368
	GMSD	0.1934	0.1953	0.1952	0.1945	0.1903	0.1908	0.1902
ESRGAN	PSNR	23.91	24.14	23.81	23.80	23.94	23.95	24.01
	SSIM	0.7322	0.7431	0.7453	0.7515	0.7662	0.7667	0.7723
	LPIPS	0.5458	0.5520	0.5437	0.5356	0.5346	0.5394	0.5371
	GMSD	0.1924	0.1944	0.1943	0.1932	0.1894	0.1904	0.1902
BSRNet	PSNR	23.61	23.87	23.60	23.62	23.70	23.77	23.86
	SSIM	0.7293	0.7419	0.7472	0.7537	0.7678	0.7698	0.7762
	LPIPS	0.5415	0.5469	0.5406	0.5375	0.5361	0.5393	0.5399
	GMSD	0.1981	0.1993	0.1988	0.1980	0.1938	0.1945	0.1933
SwinIR	PSNR	24.02	24.25	23.94	23.94	24.05	24.10	24.16
	SSIM	0.7342	0.7452	0.7479	0.7539	0.7685	0.7694	0.7755
	LPIPS	0.5436	0.5470	0.5393	0.5347	0.5342	0.5369	0.5373
	GMSD	0.1945	0.1961	0.1961	0.1951	0.1909	0.1917	0.1911
NLSN	PSNR	24.08	24.30	23.99	24.00	24.12	24.18	24.25
	SSIM	0.7347	0.7456	0.7484	0.7545	0.7692	0.7703	0.7760
	LPIPS	0.5423	0.5459	0.5379	0.5333	0.5328	0.5355	0.5356
	GMSD	0.1929	0.1950	0.1948	0.1937	0.1896	0.1902	0.1897
DASR	PSNR	24.14	24.35	24.05	24.07	24.18	24.25	24.31
	SSIM	0.7350	0.7457	0.7487	0.7547	0.7692	0.7706	0.7763
	LPIPS	0.5454	0.5490	0.5407	0.5364	0.5356	0.5382	0.5381
	GMSD	0.1923	0.1944	0.1940	0.1931	0.1892	0.1897	0.1888

Table 5.3: Evaluation results of SOTA SR networks on public and our dataset at different altitudes. Our dataset has a scale factor of 50/9, and all public datasets are downsampled according to this scale factor using the MATLAB bicubic kernel function. We upscale the networks’ output to fit our scale factor for the networks that are not pre-trained on our scale factor. We evaluate the performance using PSNR, SSIM, LPIPS, and GMSD on the Y channel in the transformed YCbCr space.

PSNR/SSIM/LPIPS		Test									
		10m	20m	30m	40m	50m	70m	80m	100m	120m	140m
Bicubic		23.12 0.7089 0.5769	22.69 0.6836 0.5959	23.39 0.6992 0.5836	24.25 0.7325 0.5694	24.41 0.7418 0.5727	24.14 0.7456 0.5633	24.16 0.7518 0.5584	24.27 0.7655 0.5572	24.34 0.7668 0.5597	24.41 0.7724 0.5581
Pretrain on Div2K		22.99 0.7111 0.5402	22.57 0.6871 0.5592	23.32 0.7036 0.5531	24.15 0.7361 0.5451	24.35 0.7461 0.5504	24.07 0.7495 0.5448	24.08 0.7557 0.5408	24.20 0.7702 0.5400	24.27 0.7716 0.5428	24.34 0.7771 0.5423
Fine-tune	All altitudes	23.38 0.7118 0.5423	22.97 0.6869 0.5639	23.60 0.6998 0.5566	24.43 0.7336 0.5484	24.58 0.7404 0.5535	24.31 0.7457 0.5473	24.32 0.7519 0.5423	24.44 0.7655 0.5415	24.52 0.7669 0.5434	24.60 0.7733 0.5421
	10m	23.44 0.7064 0.5526	23.01 0.6805 0.5767	23.61 0.6926 0.5691	24.45 0.7280 0.5583	24.56 0.7335 0.5648	24.31 0.7386 0.5581	24.32 0.7445 0.5530	24.43 0.7565 0.5530	24.48 0.7571 0.5555	24.56 0.7635 0.5537
	20m	23.40 0.7092 0.5460	22.98 0.6837 0.5678	23.61 0.6964 0.5601	24.44 0.7311 0.5505	24.57 0.7372 0.5559	24.31 0.7423 0.5503	24.32 0.7484 0.5453	24.43 0.7609 0.5449	24.50 0.7618 0.5472	24.58 0.7683 0.5456
	30m	23.36 0.7097 0.5428	22.95 0.6844 0.5643	23.59 0.6975 0.5571	24.41 0.7315 0.5483	24.56 0.7382 0.5532	24.28 0.7435 0.5473	24.29 0.7494 0.5422	24.41 0.7627 0.5416	24.48 0.7637 0.5439	24.56 0.7702 0.5424
	40m	23.36 0.7106 0.5442	22.95 0.6854 0.5659	23.59 0.6983 0.5589	24.41 0.7322 0.5498	24.56 0.7390 0.5550	24.29 0.7444 0.5484	24.30 0.7503 0.5435	24.42 0.7639 0.5426	24.49 0.7651 0.5449	24.57 0.7718 0.5433
	50m	23.36 0.7114 0.5435	22.94 0.6861 0.5649	23.59 0.6990 0.5581	24.41 0.7330 0.5494	24.56 0.7395 0.5551	24.29 0.7449 0.5486	24.30 0.7508 0.5436	24.42 0.7644 0.5425	24.49 0.7656 0.5447	24.58 0.7723 0.5432
	70m	23.34 0.7133 0.5422	22.93 0.6884 0.5625	23.58 0.7012 0.5553	24.41 0.7347 0.5479	24.57 0.7414 0.5536	24.30 0.7470 0.5469	24.31 0.7529 0.5421	24.43 0.7667 0.5408	24.50 0.7679 0.5431	24.58 0.7743 0.5414
	80m	23.35 0.7131 0.5439	22.94 0.6880 0.5645	23.58 0.7011 0.5571	24.41 0.7344 0.5497	24.57 0.7415 0.5547	24.29 0.7465 0.5486	24.31 0.7527 0.5436	24.43 0.7662 0.5421	24.50 0.7676 0.5440	24.58 0.7741 0.5426
	100m	23.33 0.7134 0.5433	22.91 0.6885 0.5633	23.57 0.7016 0.5561	24.40 0.7348 0.5489	24.55 0.7418 0.5547	24.29 0.7469 0.5482	24.30 0.7532 0.5432	24.42 0.7672 0.5419	24.49 0.7688 0.5434	24.58 0.7753 0.5422
	120m	23.33 0.7130 0.5436	22.91 0.6882 0.5637	23.57 0.7018 0.5563	24.40 0.7347 0.5496	24.55 0.7419 0.5552	24.29 0.7472 0.5487	24.30 0.7535 0.5442	24.42 0.7674 0.5428	24.50 0.7690 0.5446	24.58 0.7753 0.5434
	140m	23.34 0.7155 0.5432	22.92 0.6907 0.5631	23.58 0.7038 0.5556	24.42 0.7368 0.5484	24.58 0.7438 0.5545	24.32 0.7492 0.5478	24.33 0.7552 0.5431	24.45 0.7693 0.5419	24.53 0.7710 0.5434	24.61 0.7772 0.5422

Table 5.4: Evaluation results of fine-tuned models. We evaluate the performance using PSNR, SSIM, and LPIPS on the Y channel in the transformed YCbCr space. The best results are in bold.

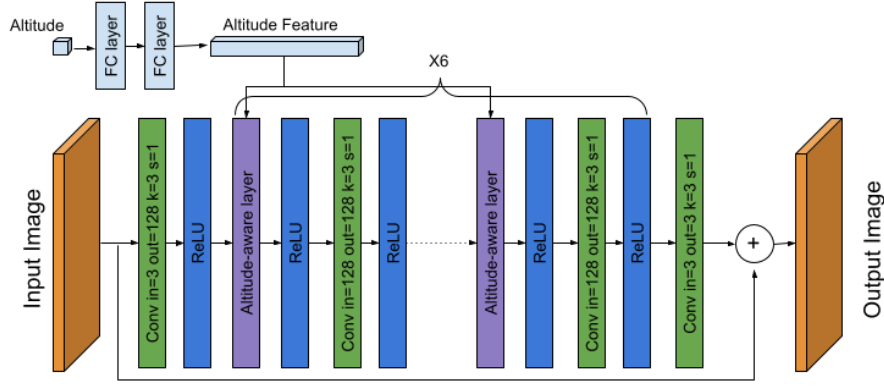
6 Robust model at varying altitudes

In this chapter, we propose two methods to build a robust SR model for varying altitudes. The most straightforward and intuitive method is feeding altitude information into the network. We present this method in Section 6.1. To make the SR models quickly to an unknown altitude, we use MAML (Finn et al., 2017) and propose a one-shot learning scheme for SR models in Section 6.2.

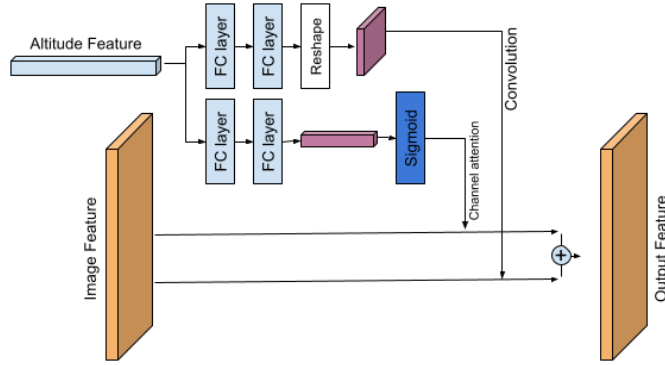
6.1 Feeding altitude information

From the previous analysis, we notice that the altitude information contributes to the performance of SR models. Since we can obtain the altitude information of each LR and HR image pair from the drone, the most intuitive method is to feed the altitude information into our network.

Inspired by internal feature manipulation techniques El Helou and Süssstrunk, 2020; Lin et al., 2021 and DASR (L. Wang, Wang, Dong, et al., 2021), we modify their degradation-aware convolutional layer to our altitude-aware convolutional layer (AAL). The AALs are used to adapt the image features conditioned on the altitude. Specifically, the altitude feature is fed into two full-connected (FC) layers and then reshaped to a convolutional kernel $w \in \mathbb{R}^{C \times 1 \times 3 \times 3}$. Next, the input image feature convolves with the obtained kernel. The resulted image feature is sent to a 1×1 convolutional layer. Meanwhile, the altitude feature is also fed into the other two FC layers, followed by a sigmoid activation to generate weights for channel-wise attention. The input image feature is processed by a channel attention operation using the generated weights. Finally, the results from depth-wise convolution and channel-wise attention are summed together to obtain the output of AAL. The detailed architecture of our AAL is shown in Figure 6.1b. We add one AAL between each standard convolutional layer in our original network. Two FC layer is added at the top of the network to encode the altitude information. The detailed architecture of our CNN network with altitude information is shown in Figure 6.1a.



(a) Overall architecture of our network with altitude information.



(b) Altitude-aware layer.

Figure 6.1: Detailed architecture of our fully convolutional network with altitude information.

We first pretrain this network under the same procedure as Section 5.3. We still use the Div2K dataset for pretraining. Div2K does not contain altitude information, so we assume all altitudes to be 1. Next, we fine-tune the network on our dataset and feed the altitude into the network. To reduce the variance of altitude, we divided the actual altitude by 80 before sending it. For fine-tuning, we train 100 epochs in total. The initial learning rate is set to be 1×10^{-5} and decreases to half every 20 epochs. We compare the performance of the proposed model with AAL and the original one in Table 6.1 and conclude that feeding altitude information into the network significantly improves SR performance.

6.2 Few-shot learning

Although we can improve drone vision performance by feeding the altitude, the train set must cover all possible evaluation altitudes. However, this is not practical in a real-world application. We cannot collect data from all possible altitudes. Updating the pretrained model quickly to adapt to a new altitude is essential. However, the naive fine-tune-based update with stochastic gradient descent (SGD) requires a large number of iterations and lots of data from

PSNR/SSIM/LPIPS	10m	20m	30m	40m	50m	70m	80m	100m	120m	140m
Bicubic	23.12 0.7089 0.5769	22.69 0.6836 0.5959	23.39 0.6992 0.5836	24.25 0.7325 0.5694	24.41 0.7418 0.5727	24.14 0.7456 0.5633	24.16 0.7518 0.5584	24.27 0.7655 0.5572	24.34 0.7668 0.5597	24.41 0.7724 0.5581
Pretrain	22.99 0.7111 0.5402	22.57 0.6871 0.5592	23.32 0.7036 0.5531	24.15 0.7361 0.5451	24.35 0.7461 0.5504	24.07 0.7495 0.5448	24.08 0.7557 0.5408	24.20 0.7702 0.5400	24.27 0.7716 0.5428	24.34 0.7771 0.5423
All altitudes	23.38 0.7118 0.5423	22.97 0.6869 0.5639	23.60 0.6998 0.5566	24.43 0.7336 0.5484	24.58 0.7404 0.5535	24.31 0.7457 0.5473	24.32 0.7519 0.5423	24.44 0.7655 0.5415	24.52 0.7669 0.5434	24.60 0.7733 0.5421
With altitude information	23.50 0.7083 0.5504	23.08 0.6850 0.5654	23.70 0.7001 0.5538	24.51 0.7344 0.5433	24.68 0.7422 0.5474	24.38 0.7483 0.5402	24.39 0.7547 0.5347	24.53 0.7700 0.5329	24.59 0.7716 0.5360	24.69 0.7787 0.5342

Table 6.1: Evaluation results of network with altitude information. "All altitudes" indicates the network mentioned in Section 5.3 and fine-tuned on all altitudes. We evaluate the performance using PSNR, SSIM, and LPIPS on the Y channel in the transformed YCbCr space. The best results are in bold.

Algorithm 1 Meta-training: one-shot

Require: f_θ : SR model with parameter θ

Require: \mathcal{L} : Loss function

Require: $\{D^1, D^2, \dots, D^H\}$: Subsets of training set at different altitude

Require: α, β : Hyper-parameters

```

1: Pretrained model  $f_\theta$ 
2: while not converge do
3:   for each  $D^h \in \{D^1, D^2, \dots, D^H\}$  do
4:     Sample 2 HR-LR pairs from  $D^h$ :  $HR_1^h, LR_1^h, HR_2^h, LR_2^h$ 
5:     Evaluate  $\nabla \mathcal{L}(f_\theta(LR_1^h, HR_1^h))$  using  $\mathcal{L}$ 
6:     Compute adapted parameters with gradient descent  $\theta^h = \theta - \alpha \nabla \mathcal{L}(f_\theta(LR_1^h, HR_1^h))$ 
7:   end for
8:   Update  $\theta = \theta - \beta \nabla_\theta \sum_{h=1}^H \mathcal{L}(f_{\theta^h}(LR_2^h, HR_2^h))$ 
9: end while

```

new altitudes.

To solve this problem, we use a meta-learning technique, MAML (Finn et al., 2017), to speed up the adaptation procedure. Firstly, we pretrain the SR networks with large external train datasets. We directly use the pretrained model in Section 5.3. Next, we start meta-learning using MAML, which optimizes the pretrained SR models to enable quick adaptation to the new task. In our dataset, we regard each altitude as an individual task, select some altitudes for meta-training, one new altitude for validation, and evaluate the other altitudes. We use FOMAML (Nichol et al., 2018) for faster training by ignoring higher-order derivatives. We use one shot, and the details procedure for meta-training is shown in the Algorithm 1. We conduct 5 gradient updates in the inner loop with a step size of $\alpha = 1 \times 10^{-5}$, and we set $\beta = 1 \times 10^{-4}$.

For inference, we randomly select one LR and HR pair from the test altitude and update the model with 5 gradient updates like training. The updated model is used for standard inference.

Train altitudes(m)	Valid altitudes(m)	10m	20m	30m	40m	50m	70m	80m	100m	120m	140m
10, 20, 30, 40, 50, 70, 80, 100	120	23.52	23.12	23.47	24.45	24.61	24.32	24.27	24.48	24.34	24.51
10, 20, 30, 40, 50, 70, 80	100	23.52	23.11	23.43	24.39	24.55	24.22	24.18	24.36	24.24	24.40
Bicubic		23.12	22.69	23.39	24.25	24.41	24.14	24.16	24.27	24.34	24.41
Pretrain on Div2K		22.99	22.57	23.32	24.15	24.35	24.07	24.08	24.20	24.27	24.34
All altitudes		23.38	22.97	23.60	24.43	24.58	24.31	24.32	24.44	24.52	24.60
With altitude information		23.50	23.08	23.70	24.51	24.68	24.38	24.39	24.53	24.59	24.69

Table 6.2: Evaluation results of one-shot learning. "All altitudes" indicates the network mentioned in Section 5.3 and fine-tuned on all altitudes. We evaluate the performance using PSNR on the Y channel in the transformed YCbCr space. The best results are in bold.

Methods	Time (sec)
Simple CNNs	3.62×10^{-3}
With altitude information	3.76×10^{-3}
One-shot learning	0.31

Table 6.3: Comparisons of the time complexity of inference for robust methods at varying altitudes of 180×180 LR image.

We evaluate the performance using different altitudes for meta-training, and the results are shown in Table 6.2. We find that the pretrained SR networks can be quickly updated to the new altitude (140m) when it is meta-trained from 10m to 100m. Although, it does not perform well when meta-trained on 10m to 80m datasets. We think the performance is limited by the size of our dataset and the complexity of our network. Nevertheless, the SR model has the potential to adapt to new altitudes efficiently after meta-training.

6.3 Analysis

Although feeding the altitude information into the network can improve image SR performance, it increases the complexity of the network, thus increasing the inference time. Besides, the SR network still needs a few steps of gradient update to fit the new altitude during the meta inference phase, which significantly boosts the inference time. We evaluate the time complexities for different methods, and the results are shown in Table 6.3. We measure time on the environment of the NVIDIA Titan X GPU. Although we only use one shot and five gradient updates for meta-inference, it is still far more time-consuming than normal inference. We also illustrate more test samples of robust models at varying altitudes in Section A.3.

6.4 Summary

We proposed two methods to build a robust SR model for varying altitudes. The first feeds altitude information into the network, and the second leverages a one-shot learning scheme, making the SR models quickly adapt to unseen altitudes. Empirical studies show that both methods are efficient. Feeding altitudes into the network improves the performance, and the

meta-trained SR network can quickly fit unseen altitudes.

7 Conclusion and future plan

In this thesis, we propose the first image SR dataset for drone vision. The LR and HR image pairs are captured by two cameras on the drone with different focal lengths. We set the same exposure value for both cameras and collected image pairs at different altitudes. After that, we propose the data preprocessing procedures to generate well-aligned HR and LR image pairs for image SR.

Extensive empirical studies show that pretrained SOTA SR networks suffer a performance drop on our dataset because the degradation model used to train those networks is far simpler than ours. The performance of SR networks varies among altitudes, and we also observe images captured at lower altitudes contain more high-frequency details. Then, we conclude that domain gaps exist among LR and HR pairs from different altitudes.

Finally, we propose two methods to build a robust SR model at varying altitudes. The first feeds altitude information into the network through altitude-aware layers. The second uses one-shot learning to adapt the SR model quickly to unknown altitudes. Experiments show the proposed method can efficiently improve the performance of SR networks at varying altitudes. However, the SR network used in this thesis is very simple, and more complex SR networks remain in our future research.

As an essential technique in computer vision and image processing, image SR can improve other downstream tasks, such as classification and segmentation, which are widely used in many drone applications. Therefore, the benefit of drone base SR on other drone vision tasks can be explored in the future. On the other hand, datasets are critical for learning-based computer vision techniques. Our dataset contains burst LR sequences and RAW data, which benefits further research. We believe our dataset will encourage more researchers to delve into image SR for drone vision.

A More visual examples

A.1 SR matching visualisation

A.2 Test samples of fine-tuning

A.3 Test samples of robust model for varying altitudes

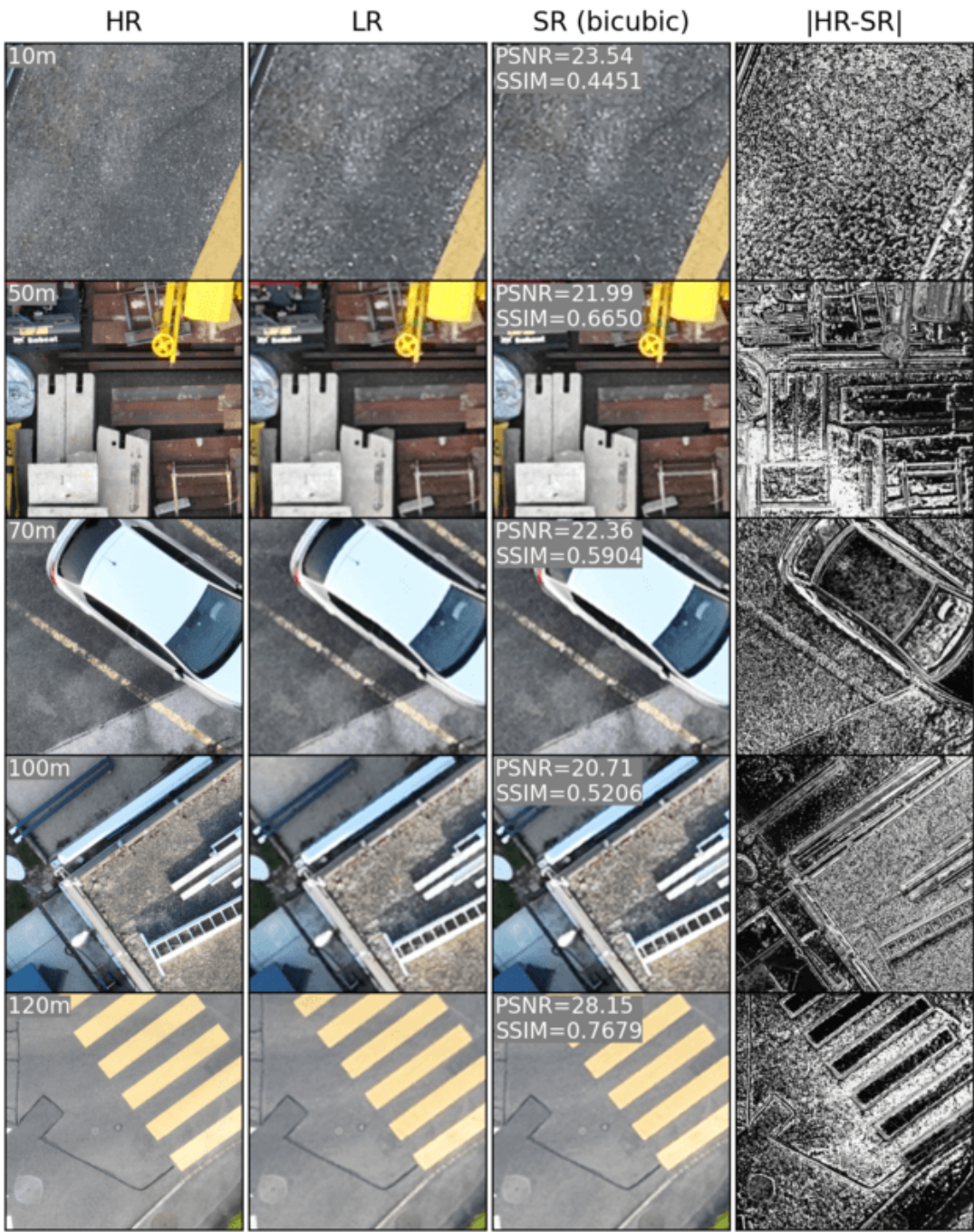
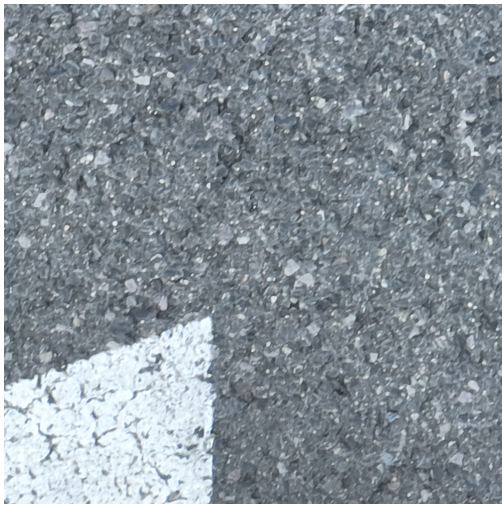
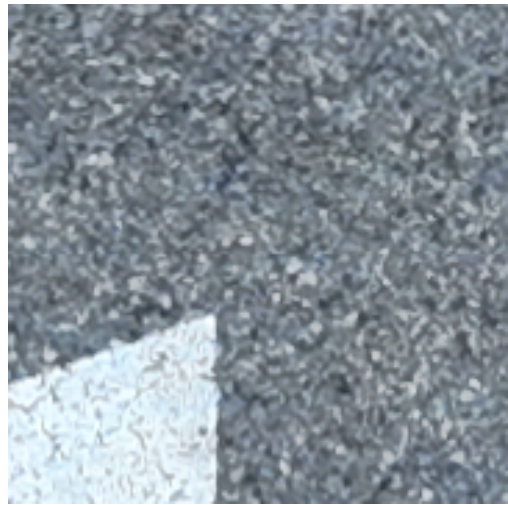


Figure A.1: Visualisation of mismatching between HR and SR images.



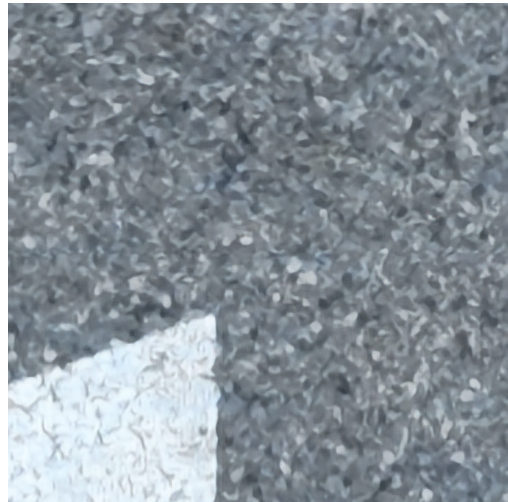
(a) HR



(b) LR



(c) Pretrain (PSNR: 21.64, SSIM: 0.6709)



(d) Fine-tune on all altitudes (PSNR: 22.13, SSIM: 0.6517)



(e) Fine-tune on 10m (PSNR: 22.15, SSIM: 0.6433)



(f) Fine-tune on 140m (PSNR: 22.09, SSIM: 0.6622)

Figure A.2: Test sample at 10m altitude



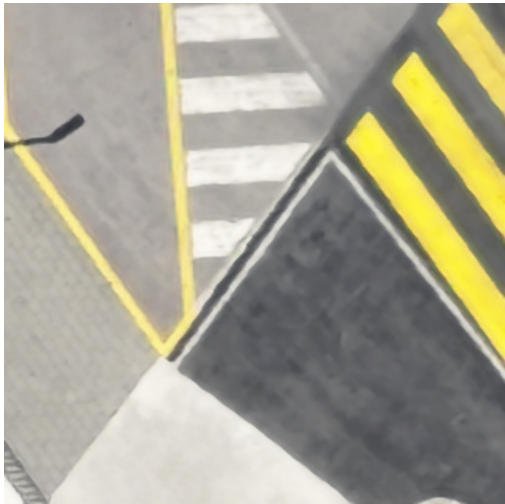
(a) HR



(b) LR



(c) Pretrain (PSNR: 27.31, SSIM: 0.8557)



(d) Fine-tune on all altitudes (PSNR: 27.75, SSIM: 0.8698)



(e) Fine-tune on 10m (PSNR: 27.42, SSIM: 0.8613)



(f) Fine-tune on 140m (PSNR: 27.80, SSIM: 0.8701)

Figure A.3: Test sample at 140m altitude



(a) HR



(b) LR



(c) Without altitudes info (PSNR: 22.77, SSIM: 0.7349)



(d) With altitude info (PSNR: 22.79, SSIM: 0.7390)

Figure A.4: Test sample at 80m altitude

Bibliography

- Afifi, M., Price, B., Cohen, S., & Brown, M. S. (2019). When color constancy goes wrong: correcting improperly white-balanced images. *Proceedings of the IEEE/CVF Conference on Computer Vision and Pattern Recognition*, 1535–1544.
- Agustsson, E., & Timofte, R. (2017). Ntire 2017 challenge on single image super-resolution: dataset and study. *Proceedings of the IEEE Conference on Computer Vision and Pattern Recognition Workshops*, 126–135.
- Akbari, Y., Almaadeed, N., Al-Maadeed, S., & Elharrouss, O. (2021). Applications, databases and open computer vision research from drone videos and images: a survey. *Artificial Intelligence Review*, 54(5), 3887–3938.
- Al-Kaff, A., Martin, D., Garcia, F., de la Escalera, A., & Armingol, J. M. (2018). Survey of computer vision algorithms and applications for unmanned aerial vehicles. *Expert Systems with Applications*, 92, 447–463.
- Bevilacqua, M., Roumy, A., Guillemot, C., & Alberi-Morel, M. L. (2012). Low-complexity single-image super-resolution based on nonnegative neighbor embedding.
- Bhat, G., Danelljan, M., Van Gool, L., & Timofte, R. (2021). Deep burst super-resolution. *Proceedings of the IEEE/CVF Conference on Computer Vision and Pattern Recognition*, 9209–9218.
- Cai, J., Gu, S., Timofte, R., & Zhang, L. (2019). Ntire 2019 challenge on real image super-resolution: methods and results. *Proceedings of the IEEE Conference on Computer Vision and Pattern Recognition Workshops*.
- Cai, J., Zeng, H., Yong, H., Cao, Z., & Zhang, L. (2019). Toward real-world single image super-resolution: a new benchmark and a new model. *Proceedings of the IEEE International Conference on Computer Vision*.
- Chang, H., Yeung, D.-Y., & Xiong, Y. (2004). Super-resolution through neighbor embedding. *Proceedings of the IEEE Computer Society Conference on Computer Vision and Pattern Recognition*, 1, I–I.
- Dong, C., Loy, C. C., He, K., & Tang, X. (2014). Learning a deep convolutional network for image super-resolution. *Proceedings of the European Conference on Computer Vision*, 184–199.
- Du, D., Qi, Y., Yu, H., Yang, Y., Duan, K., Li, G., Zhang, W., Huang, Q., & Tian, Q. (2018). The unmanned aerial vehicle benchmark: object detection and tracking. *Proceedings of the European Conference on Computer Vision*, 370–386.

- Dudhane, A., Zamir, S. W., Khan, S., Khan, F., & Yang, M.-H. (2021). Burst image restoration and enhancement. *arXiv preprint arXiv:2110.03680*.
- El Helou, M. (2021). *Deep image restoration: between data fidelity and learned priors* (tech. rep.). EPFL.
- El Helou, M., & Ssstrunk, S. (2020). Blind universal Bayesian image denoising with Gaussian noise level learning. *IEEE Transactions on Image Processing*, 29, 4885–4897.
- El Helou, M., & Ssstrunk, S. (2022). BIGPrior: toward decoupling learned prior hallucination and data fidelity in image restoration. *IEEE Transactions on Image Processing*, 31, 1628–1640.
- El Helou, M., Zhou, R., & Ssstrunk, S. (2020). Stochastic frequency masking to improve super-resolution and denoising networks. *Proceedings of the European Conference on Computer Vision*, 749–766.
- Evangelidis, G. D., & Psarakis, E. Z. (2008). Parametric image alignment using enhanced correlation coefficient maximization. *IEEE Transactions on Pattern Analysis and Machine Intelligence*, 30(10), 1858–1865.
- Finn, C., Abbeel, P., & Levine, S. (2017). Model-agnostic meta-learning for fast adaptation of deep networks. *Proceedings of the International Conference on Machine learning*, 1126–1135.
- Fischler, M. A., & Bolles, R. C. (1981). Random sample consensus: a paradigm for model fitting with applications to image analysis and automated cartography. *Communications of the ACM*, 24(6), 381–395.
- Gu, J., Lu, H., Zuo, W., & Dong, C. (2019). Blind super-resolution with iterative kernel correction. *Proceedings of the IEEE/CVF Conference on Computer Vision and Pattern Recognition*, 1604–1613.
- Hsieh, M.-R., Lin, Y.-L., & Hsu, W. H. (2017). Drone-based object counting by spatially regularized regional proposal network. *Proceedings of the IEEE International Conference on Computer Vision*, 4145–4153.
- Hu, X., Mu, H., Zhang, X., Wang, Z., Tan, T., & Sun, J. (2019). Meta-sr: a magnification-arbitrary network for super-resolution. *Proceedings of the IEEE/CVF Conference on Computer Vision and Pattern Recognition*, 1575–1584.
- Huang, J.-B., Singh, A., & Ahuja, N. (2015). Single image super-resolution from transformed self-exemplars. *Proceedings of the IEEE conference on Computer Vision and Pattern Recognition*, 5197–5206.
- Jolicoeur-Martineau, A. (2018). The relativistic discriminator: a key element missing from standard gan. *arXiv preprint arXiv:1807.00734*.
- Karras, T., Laine, S., & Aila, T. (2019). A style-based generator architecture for generative adversarial networks. *Proceedings of the IEEE/CVF Conference on Computer Vision and Pattern Recognition*, 4401–4410.
- Kim, J., Lee, J. K., & Lee, K. M. (2016a). Accurate image super-resolution using very deep convolutional networks. *Proceedings of the IEEE Conference on Computer Vision and Pattern Recognition*, 1646–1654.

- Kim, J., Lee, J. K., & Lee, K. M. (2016b). Deeply-recursive convolutional network for image super-resolution. *Proceedings of the IEEE Conference on Computer Vision and Pattern Recognition*, 1637–1645.
- Kingma, D. P., & Ba, J. (2014). Adam: a method for stochastic optimization. *arXiv preprint arXiv:1412.6980*.
- Lecouat, B., Ponce, J., & Mairal, J. (2021). Lucas-kanade reloaded: end-to-end super-resolution from raw image bursts. *Proceedings of the IEEE/CVF International Conference on Computer Vision*, 2370–2379.
- Liang, J., Cao, J., Sun, G., Zhang, K., Van Gool, L., & Timofte, R. (2021). Swinir: image restoration using swin transformer. *Proceedings of the IEEE/CVF International Conference on Computer Vision*, 1833–1844.
- Liang, Q., Cassayre, F., Owsianko, H., El Helou, M., & Süsstrunk, S. (2022). Image denoising with control over deep network hallucination. *arXiv preprint arXiv:2201.00429*.
- Lim, B., Son, S., Kim, H., Nah, S., & Mu Lee, K. (2017). Enhanced deep residual networks for single image super-resolution. *Proceedings of the IEEE Conference on Computer Vision and Pattern Recognition Workshops*, 136–144.
- Lin, X., Bhattacharjee, D., El Helou, M., & Süsstrunk, S. (2021). Fidelity estimation improves noisy-image classification with pretrained networks. *IEEE Signal Processing Letters*, 28, 1719–1723.
- Liu, K., & Mattyus, G. (2015). Fast multiclass vehicle detection on aerial images. *IEEE Geoscience and Remote Sensing Letters*, 12(9), 1938–1942.
- Lowe, D. G. (1999). Object recognition from local scale-invariant features. *Proceedings of IEEE International Conference on Computer Vision*, 2, 1150–1157.
- Ma, K., Duanmu, Z., Wu, Q., Wang, Z., Yong, H., Li, H., & Zhang, L. (2016). Waterloo exploration database: new challenges for image quality assessment models. *IEEE Transactions on Image Processing*, 26(2), 1004–1016.
- Martin, D., Fowlkes, C., Tal, D., & Malik, J. (2001). A database of human segmented natural images and its application to evaluating segmentation algorithms and measuring ecological statistics. *Proceedings of the IEEE International Conference on Computer Vision*, 2, 416–423.
- Mei, Y., Fan, Y., & Zhou, Y. (2021). Image super-resolution with non-local sparse attention. *Proceedings of the IEEE/CVF Conference on Computer Vision and Pattern Recognition*, 3517–3526.
- Nichol, A., Achiam, J., & Schulman, J. (2018). On first-order meta-learning algorithms. *arXiv preprint arXiv:1803.02999*.
- Oh, S., Hoogs, A., Perera, A., Cuntoor, N., Chen, C.-C., Lee, J. T., Mukherjee, S., Aggarwal, J., Lee, H., Davis, L., et al. (2011). A large-scale benchmark dataset for event recognition in surveillance video. *CVPR 2011*, 3153–3160.
- Park, S., Yoo, J., Cho, D., Kim, J., & Kim, T. H. (2020). Fast adaptation to super-resolution networks via meta-learning. *Proceedings of the European Conference on Computer Vision*, 754–769.

- Shocher, A., Cohen, N., & Irani, M. (2018). “zero-shot” super-resolution using deep internal learning. *Proceedings of the IEEE Conference on Computer Vision and Pattern Recognition*, 3118–3126.
- Soh, J. W., Cho, S., & Cho, N. I. (2020). Meta-transfer learning for zero-shot super-resolution. *Proceedings of the IEEE/CVF Conference on Computer Vision and Pattern Recognition*.
- Tai, Y., Yang, J., & Liu, X. (2017). Image super-resolution via deep recursive residual network. *Proceedings of the IEEE Conference on Computer Vision and Pattern Recognition*, 3147–3155.
- Tai, Y., Yang, J., Liu, X., & Xu, C. (2017). Memnet: a persistent memory network for image restoration. *Proceedings of the IEEE International Conference on Computer Vision*, 4539–4547.
- Timofte, R., Agustsson, E., Van Gool, L., Yang, M.-H., & Zhang, L. (2017). Ntire 2017 challenge on single image super-resolution: methods and results. *Proceedings of the IEEE Conference on Computer Vision and Pattern Recognition Workshops*, 114–125.
- Timofte, R., De Smet, V., & Van Gool, L. (2013). Anchored neighborhood regression for fast example-based super-resolution. *Proceedings of the IEEE International Conference on Computer Vision*, 1920–1927.
- Wang, L., Wang, Y., Dong, X., Xu, Q., Yang, J., An, W., & Guo, Y. (2021). Unsupervised degradation representation learning for blind super-resolution. *Proceedings of the IEEE/CVF Conference on Computer Vision and Pattern Recognition*, 10581–10590.
- Wang, L., Wang, Y., Lin, Z., Yang, J., An, W., & Guo, Y. (2021). Learning a single network for scale-arbitrary super-resolution. *Proceedings of the IEEE/CVF International Conference on Computer Vision*, 4801–4810.
- Wang, X., Yu, K., Wu, S., Gu, J., Liu, Y., Dong, C., Qiao, Y., & Change Loy, C. (2018). Esrgan: enhanced super-resolution generative adversarial networks. *Proceedings of the European Conference on Computer Vision Workshops*.
- Wang, Z., Bovik, A. C., Sheikh, H. R., & Simoncelli, E. P. (2004). Image quality assessment: from error visibility to structural similarity. *IEEE Transactions on Image Processing*, 13(4), 600–612.
- Xu, X., Zhang, X., Yu, B., Hu, X. S., Rowen, C., Hu, J., & Shi, Y. (2019). Dac-sdc low power object detection challenge for uav applications. *IEEE Transactions on Pattern Analysis and Machine Intelligence*, 43(2), 392–403.
- Xu, Y., Ou, J., He, H., Zhang, X., & Mills, J. (2016). Mosaicking of unmanned aerial vehicle imagery in the absence of camera poses. *Remote Sensing*, 8(3), 204.
- Xue, W., Zhang, L., Mou, X., & Bovik, A. C. (2013). Gradient magnitude similarity deviation: a highly efficient perceptual image quality index. *IEEE Transactions on Image Processing*, 23(2), 684–695.
- Yu, H., Li, G., Zhang, W., Huang, Q., Du, D., Tian, Q., & Sebe, N. (2020). The unmanned aerial vehicle benchmark: object detection, tracking and baseline. *International Journal of Computer Vision*, 128(5), 1141–1159.
- Zeyde, R., Elad, M., & Protter, M. (2010). On single image scale-up using sparse-representations. *International Conference on Curves and Surfaces*, 711–730.

- Zhang, K., Liang, J., Van Gool, L., & Timofte, R. (2021). Designing a practical degradation model for deep blind image super-resolution. *IEEE International Conference on Computer Vision*, 4791–4800.
- Zhang, R., Isola, P., Efros, A. A., Shechtman, E., & Wang, O. (2018). The unreasonable effectiveness of deep features as a perceptual metric. *Proceedings of the IEEE Conference on Computer Vision and Pattern Recognition*, 586–595.
- Zhang, X., Chen, Q., Ng, R., & Koltun, V. (2019). Zoom to learn, learn to zoom. *Proceedings of the IEEE/CVF Conference on Computer Vision and Pattern Recognition*, 3762–3770.
- Zhang, Y., Li, K., Li, K., Wang, L., Zhong, B., & Fu, Y. (2018). Image super-resolution using very deep residual channel attention networks. *Proceedings of the European Conference on Computer Vision*, 286–301.
- Zhang, Y., Tian, Y., Kong, Y., Zhong, B., & Fu, Y. (2018). Residual dense network for image super-resolution. *Proceedings of the IEEE Conference on Computer Vision and Pattern Recognition*, 2472–2481.
- Zhou, R., El Helou, M., Sage, D., Laroche, T., Seitz, A., & Süssstrunk, S. (2020). W2S: microscopy data with joint denoising and super-resolution for Widefield to SIM mapping. *Proceedings of the European Conference on Computer Vision*, 474–491.
- Zhou, R., Lahoud, F., El Helou, M., & Süssstrunk, S. (2019). A comparative study on wavelets and residuals in deep super resolution. *Electronic Imaging*.
- Zhu, P., Wen, L., Du, D., Bian, X., Ling, H., Hu, Q., Wu, H., Nie, Q., Cheng, H., Liu, C., et al. (2018). Visdrone-vdt2018: the vision meets drone video detection and tracking challenge results. *Proceedings of the European Conference on Computer Vision Workshops*.